

# ABSTRACT

Title of Dissertation: NUMERICAL MODELING OF MULTIPHASE  
EXPLOSIONS

Thomas P. McGrath II, Doctor of Philosophy, 2008

Directed by: Dr. Gregory S. Jackson  
Dept. of Mechanical Engineering

This work describes the development and application of a compressible multiphase flow model for the numerical simulation of multiphase explosions containing a dispersed particle phase. The model treats all phases as fully compressible, allows full non-equilibrium among phases, and properly models the mathematical characteristics of a dispersed particle phase in both the dense and dilute limits. Using the characteristic equations, a multiphase Riemann solver is developed as the basis for a Godunov-based numerical method. The Riemann solver is approximate, non-iterative, and applicable to all phases. A heuristic equation of state modeling the functional dependence of the dispersed phase pressure on volume fraction is proposed and applied. Using the techniques developed, two multiphase explosion simulations are performed and compared with experiment. Excellent agreement between the numerical and experimental results is found, providing confidence in the solution techniques developed. The sensitivity of the model to correlations for drag, heat transfer, and dispersed phase pressure are also investigated. Results from this analysis indicate that the functional dependence of

dispersed phase pressure on volume fraction must be properly represented to obtain accurate simulation results in scenarios where particle-particle interactions are important. Further analyses investigate the effects of physical parameters including particle loading, size, and material on multiphase explosion dynamics. The results of this study indicate the significant effect these parameters have on the overall explosion dynamics, which is important to applications involving both inert and reactive particles.

# NUMERICAL MODELING OF MULTIPHASE EXPLOSIONS

by

Thomas P. McGrath II

Dissertation submitted to the Faculty of the Graduate School of the  
University of Maryland, College Park, in partial fulfillment  
of the requirements for the degree of  
Doctor of Philosophy  
2008

Advisory Committee:  
Professor Gregory S. Jackson, Chair  
Professor Kenneth Kiger  
Professor Arnaud Trouvé  
Professor Jerry Forbes  
Professor James Baeder

© Copyright by  
Thomas P. McGrath II  
2008

# Dedication

To Carmel,

for sacrificing as much as I did in pursuit of this goal.

## Acknowledgments

The author first wishes to thank Dr. Andrew Wardlaw for sharing his advice and expertise in the field of numerical model development, as well as his considerable theoretical insight into the physics of compressible flows. The author would also like to thank Dr. Joel Carney and Dr. James Lightstone for providing the data from their PETN/glass experiments conducted at NSWC Indian Head. Finally, the author wishes to thank both Mr. Robert Kavetsky and the Indian Head Core Research program for recognizing the importance of this work and funding this research.

# Table of Contents

<b>Dedication</b>	<b>ii</b>
<b>Acknowledgments</b>	<b>iii</b>
<b>Table of Contents</b>	<b>iv</b>
<b>List of Tables</b>	<b>vi</b>
<b>List of Figures</b>	<b>vii</b>
<b>1 Introduction</b>	<b>1</b>
1.1 Motivation . . . . .	2
1.2 Previous Work . . . . .	3
1.3 Statement of Work . . . . .	6
<b>2 Governing Equations</b>	<b>9</b>
2.1 Derivation of Governing Equations . . . . .	9
2.1.1 Continuity Equation . . . . .	10
2.1.2 Momentum Equation . . . . .	11
2.1.3 Energy Equation . . . . .	13
2.1.4 Number Density Equation . . . . .	15
2.1.5 Convected Variable Equation . . . . .	15
2.1.6 Volume Fraction Equation . . . . .	15
2.2 Multiphase Equations in Differential Form . . . . .	17
2.3 Discussion . . . . .	18
2.3.1 Dispersed Phase Material Modeling . . . . .	19
2.3.2 Discussion of Nozzling Terms . . . . .	21
2.4 Results of Characteristic Analysis . . . . .	24
<b>3 Numerical Model Development</b>	<b>26</b>
3.1 Convective Operator Solution . . . . .	27
3.2 Source Term Operator Solution . . . . .	36
3.3 Dispersed Phase Equation of State . . . . .	40

<b>4</b>	<b>Comparison with Experiment</b>	<b>43</b>
4.1	Multiphase Explosion Simulation #1 . . . . .	44
4.2	Multiphase Explosion Simulation #2 . . . . .	50
<b>5</b>	<b>Sensitivity to Correlations for Drag, Heat Transfer, and Dispersed Phase Pressure</b>	<b>55</b>
5.1	Sensitivity to Drag Correlations . . . . .	56
5.2	Sensitivity to Heat Transfer . . . . .	61
5.3	Sensitivity to Dispersed Phase Pressure . . . . .	64
5.3.1	Sensitivity to Dispersed Phase Pressure Representation . . .	65
5.3.2	Sensitivity to $\alpha_{max}, \alpha_{min}$ , and $z$ . . . . .	69
<b>6</b>	<b>Effect of Physical Parameters on Multiphase Explosions</b>	<b>77</b>
6.1	Effect of Particle Loading . . . . .	78
6.2	Effect of Particle Diameter . . . . .	85
6.3	Effect of Particle Material . . . . .	93
<b>7</b>	<b>Conclusions and Future Work</b>	<b>97</b>
<b>A</b>	<b>Characteristic Analysis</b>	<b>102</b>
	<b>Bibliography</b>	<b>106</b>

## List of Tables

2.1	Coordinate System Geometries . . . . .	17
5.1	Maximum particle temperatures calculated using various heat transfer rates . . . . .	62
6.1	Particle volume and mass fractions investigated in Sec. 6.1 . . . . .	79
6.2	Particle material properties . . . . .	93

## List of Figures

2.1	Eulerian control volume containing multiphase flow. . . . .	10
3.1	Generic Riemann structure for two-phase flow. . . . .	29
3.2	Possible locations of the volume fraction discontinuity within the Riemann structure for any given phase. . . . .	30
3.3	Structure of approximate Riemann solution for any single phase. . .	32
3.4	Structure of Riemann solution for hyperbolically degenerate systems.	34
3.5	Structure of approximate Riemann solution for a two-phase flow before volume fraction inconsistency fix. . . . .	36
4.1	Velocity and volume fraction profiles at 0.25 <i>ms</i> for explosion of nitromethane charge with 463 $\mu m$ steel particles; 62% initial particle loading by volume. . . . .	46
4.2	Velocity and volume fraction profiles at 0.50 <i>ms</i> for explosion of nitromethane charge with 463 $\mu m$ steel particles; 62% initial particle loading by volume. . . . .	47
4.3	Velocity and volume fraction profiles at 1.00 <i>ms</i> for explosion of nitromethane charge with 463 $\mu m$ steel particles; 62% initial particle loading by volume. . . . .	47
4.4	Velocity and volume fraction profiles at 2.00 <i>ms</i> for explosion of nitromethane charge with 463 $\mu m$ steel particles; 62% initial particle loading by volume. . . . .	48
4.5	Comparison of experimental and numerical shock and particle front locations from the detonation of a nitromethane charge with 463 $\mu m$ steel particles; 62% initial particle loading by volume. . . . .	49
4.6	Comparison of experimental and numerical peak pressures from pure nitromethane and nitromethane/steel particle explosions. . . . .	50
4.7	Comparison of numerical contours and experimental image 10 $\mu s$ after explosion of PETN charge with 10 $\mu m$ glass particles. Numerical results include contours of particle volume fraction ( $\alpha_D$ ), solid line indicating shock front, and dashed line indicating detonation product front. Dashed white line indicates initial charge geometry. .	52

4.8	Comparison of numerical contours and experimental image 20 $\mu s$ after explosion of PETN charge with 10 $\mu m$ glass particles. Numerical results include contours of particle volume fraction ( $\alpha_D$ ), solid line indicating shock front, and dashed line indicating detonation product front. Dashed white line indicates initial charge geometry. . . . .	53
4.9	Comparison of experimental and numerical particle front trajectories broadside of PETN/glass particle explosion. . . . .	54
5.1	Comparison of drag force correlations. . . . .	58
5.2	Effect of drag correlations on shock propagation, peak pressure, and particle front location. . . . .	60
5.3	Effect of heat transfer on shock propagation, peak pressure, and particle front location. . . . .	63
5.4	Effect of dispersed phase pressure on shock propagation, peak pressure, and particle front location. . . . .	67
5.5	Profiles of pressure and particle volume fraction for the case of $P_D = \zeta(\alpha_D) P_{int,D}$ . Dotted line indicates threshold volume fraction. . . . .	68
5.6	Functional dependence of $\zeta$ with respect to $\alpha_{max}$ , $\alpha_{min}$ , and $z$ . . . . .	70
5.7	Effect of $\alpha_{max}$ on shock propagation, peak pressure, and particle front location. . . . .	72
5.8	Effect of $\alpha_{min}$ on shock propagation, peak pressure, and particle front location. . . . .	74
5.9	Effect of $z$ on shock propagation, peak pressure, and particle front location. . . . .	76
6.1	Effect of initial particle loading on shock front motion. . . . .	80
6.2	Effect of initial particle loading on peak pressure. . . . .	80
6.3	Effect of initial particle loading on particle front motion. . . . .	81
6.4	Effect of initial particle loading on detonation product front motion. . . . .	81
6.5	Velocity and volume fraction profiles at 0.25 $ms$ for explosion of nitromethane charge with 463 $\mu m$ steel particles; 15% initial particle loading by volume. . . . .	83
6.6	Velocity and volume fraction profiles at 1.00 $ms$ for explosion of nitromethane charge with 463 $\mu m$ steel particles; 15% initial particle loading by volume. . . . .	83
6.7	Shock, particle, and detonation front trajectories from nitromethane charge with 46.3 $\mu m$ steel particles; 62% particles by volume. . . . .	86
6.8	Shock, particle, and detonation front trajectories from nitromethane charge with 463 $\mu m$ steel particles; 62% particles by volume. . . . .	86
6.9	Velocity and volume fraction profiles at 0.50 $ms$ for explosion of nitromethane charge with 46.3 $\mu m$ steel particles; 62% initial particle loading by volume. . . . .	87

6.10	Velocity and volume fraction profiles at 2.00 <i>ms</i> for explosion of nitromethane charge with 46.3 $\mu m$ steel particles; 62% initial particle loading by volume. . . . .	88
6.11	Temperature profiles at 0.50 <i>ms</i> for explosions of nitromethane charges with 46.3 and 463 $\mu m$ steel particles; 62% initial particle loading by volume. . . . .	90
6.12	Temperature profiles at 2.00 <i>ms</i> for explosions of nitromethane charges with 46.3 and 463 $\mu m$ steel particles; 62% initial particle loading by volume. . . . .	90
6.13	Peak shock pressures from explosions of nitromethane charges with 46.3 and 463 $\mu m$ steel particles; 62% initial particle loading by volume.	91
6.14	Shock, particle, and detonation front trajectories from nitromethane charge with 46.3 $\mu m$ steel particles; 15% initial particle loading by volume. . . . .	92
6.15	Shock, particle, and detonation front trajectories from nitromethane charge with 463 $\mu m$ steel particles; 15% initial particle loading by volume. . . . .	92
6.16	Shock, particle, and detonation front trajectories from nitromethane charge with 463 $\mu m$ glass particles; 62% initial particle loading by volume. . . . .	94
6.17	Peak pressures from nitromethane charges with 463 $\mu m$ steel or glass particles; 62% initial particle loading by volume. . . . .	94
6.18	Velocity and volume fraction profiles at 0.50 <i>ms</i> for explosion of nitromethane charge with 463 $\mu m$ glass particles; 62% initial particle loading by volume. . . . .	96
6.19	Velocity and volume fraction profiles at 2.00 <i>ms</i> for explosion of nitromethane charge with 463 $\mu m$ glass particles; 62% initial particle loading by volume. . . . .	96

# Chapter 1

## Introduction

This work proposes, develops, and applies a compressible multiphase flow model for the numerical simulation of multiphase explosions. Compressible multiphase flow modeling is not as well developed as its single-phase counterpart, and a need to improve existing techniques clearly exists. The numerical model developed in this work distinguishes itself from others in the literature by: 1) treating all phases as fully compressible, 2) properly representing the mathematical characteristics of dispersed particle phases in the both the dense and dilute limits, 3) applying a Godunov-based solution to all phases, and 4) allowing complete non-equilibrium among phases. Results from numerical simulations validate the model against existing experimental data, and reveal fundamental information on the physical nature of dispersed phases and the modeling approaches necessary to treat them. Additional results investigate the sensitivity of the numerical model to correlations for drag and heat transfer, as well as physical parameters including particle loading, size, and material. The compilation of these efforts provides important fundamental information necessary for accurately understanding and modeling multiphase explosions, as well as for designing/analyzing systems utilizing them.

## 1.1 Motivation

Multiphase explosions occurring in heterogeneous materials consisting of a dispersed particle phase embedded in an explosive or otherwise reactive media are of considerable interest to the combustion, energetic material development, propulsion, and hazard/risk assessment communities. Examples of multiphase explosion events include coal dust explosions, supersonic combustion of metal-laden fuels, deflagration-to-detonation transition in granular energetic materials, and the detonation of metalized high-explosive formulations. Yet, despite widespread interest and practical application, much about the dynamics of multiphase explosions remains unknown. The very high temperatures and pressures of explosion events, coupled with the complex physical processes occurring due to the multiphase nature of the flow, make experimental investigations of these events difficult. During the explosion, particles can become high-speed projectiles that complicate traditional pressure measurements and destroy instrumentation. The particles can also reduce optical clarity, inhibiting the effectiveness of optical diagnostic techniques. Because of the experimental difficulties, numerical modeling is an attractive option for investigating the dynamics of multiphase explosions.

When examining the literature relating to numerical modeling of multiphase explosions, it is clear that the field is relatively young and work remains. Compressible multiphase flows have not historically received as much attention in the modeling community as their single-phase and incompressible counterparts, and the complexities of phase interactions combined with compressibility present considerable conceptual challenges. Perhaps the best indication of this is that to date no universally accepted set of governing equations exists. Much of the debate concerning the governing equations is centered around the existence and form of the nozzling terms, which are discussed in Sec. 2.3.2. Disagreement also exists over

the physical nature and treatment of dispersed materials, which are a major focus of the current work.

The following section discusses previous work relating to the numerical modeling of multiphase explosions. It provides a synopsis of five of the most influential papers relating to this field, and identifies the distinguishing features of each. While each work makes a unique contribution, none are completely satisfactory. Improving on these models to develop a robust, accurate, and consistent modeling approach is the motivation for the current work.

## 1.2 Previous Work

Perhaps the most influential work relating to multiphase explosion modeling is the study of deflagration-to-detonation transition (DDT) in reactive granular materials published by Baer and Nunziato [1]. Using arguments based on thermodynamic constraints, Baer and Nunziato proposed a system of governing equations for a reactive two-phase flow in granular explosives. This model treats both phases as fully compressible, and allows for complete non-equilibrium between the phases. To close the system of equations, a dynamic compaction equation governing the evolution of volume fraction was introduced. The dynamic compaction equation eliminated the need for the assumption of pressure equilibrium, which when rigidly applied can cause the equations to become ill-posed [1]. Numerical solution of the governing equations was accomplished with a standard artificial viscosity method, as can be applied to the Euler equations. Since its publication, many of the fundamental principals of the Baer and Nunziato model [1] have been adopted in subsequent works involving compressible multiphase flows.

Another notable work relating to the numerical modeling of DDT is that of Gonthier and Powers [10]. This paper presents a Godunov-based numerical method

for a reactive two-phase flow. The governing equations used were similar to those of Baer and Nunziato [1] without the nozzling terms. The nozzling terms are a source of debate in the literature, and are further discussed in Sec. 2.3.2 of this work. Gonthier and Powers [10] develop a Roe-type [23, 24] approximate Riemann solver for the two-phase flow equations, which forms the basis of a higher-order Godunov-type numerical method. Apart from the nozzling terms, the application of a high-resolution Godunov-type method is the distinguishing feature between this work and that of Baer and Nunziato [1].

Saurel and Lemetayer [25] proposed a generalization of Baer and Nunziato’s model [1] to a system involving more than two phases. Using these equations, they present a numerical solution technique aimed at computing both multifluid and multiphase problems. Multifluid problems are distinguished from multiphase problems in that the various phases are discretized on the grid in a multifluid problem, while in multiphase problems they are not. The key difference separating the model proposed by Saurel and Lemetayer [25] from that of Baer and Nunziato [1] resides in the treatment of the relaxation terms. Saurel and Lemetayer introduce infinite relaxation parameters for pressure and velocity, which enforce pressure and velocity equilibrium among phases. Under this assumption, they introduce a Godunov-based solution using the HLL [12] Riemann solver, while solving for the non-conservative terms in a method that retains pressure and velocity equilibrium. While the assumption of pressure equilibrium is often justified in multiphase explosion modeling (as discussed in Sec. 3.2), the assumption of velocity equilibrium is not. Velocity non-equilibrium is, in fact, a critical feature in many multiphase explosion scenarios, necessitating a numerical method accounting for these effects.

An important feature common to the models discussed above [1, 10, 25] as well as others [2, 13] lies in the treatment of the dispersed phase pressure. These models assume that the pressure of a dispersed phase is equal to that of the con-

stituent material of the individual particles or grains. This assumption may be justified in the case of densely-packed granular flows, but is not valid in general. Rather, as particles separate and the flow becomes dilute, the pressure and sound speed of a dispersed phase goes to zero [4, 8, 32]. This lack of pressure and sound speed modifies the mathematical characteristics of the governing equations, which affects the numerical solution. Properly representing the mathematical characteristics of the governing equations, and developing an accurate solution technique is a major motivation for the current work.

Papalexandris [17, 18] developed a numerical model for studying the effects of inert and reactive particles on detonation waves in gases. Because the work focused on gases mixed with stiff particles, the particle material was assumed to be incompressible. Additionally, the model focused exclusively on scenarios involving dilute collections of particles. Because of this, no pressure force was included in the governing equation for the particle phase. The lack of pressure in the dispersed phase equations further implies that the phase has zero sound speed, making the particle phase equations hyperbolically degenerate. Given this, Papalexandris [17] appropriately modifies the numerical solution for the particle phase. This work provides useful insight into the development of numerical methods for multiphase flows; however, the assumptions of incompressible particles and dilute flows are unattractive for more general modeling purposes, necessitating further work.

Zhang, et al. [32] presented a numerical and experimental investigation of the explosive dispersal of solid particles. The governing equations used in this study were proposed to extend the Baer and Nunziato [1] model to dilute particle flows. Here, a heuristic equation of state for the dispersed particle phase was applied such that the particle phase pressure is a function of the particle volume fraction. This is again based on the physical argument that the pressure of a collection of particles is a function of particle spacing. Using the modified model,

Zhang et al. [32] applied a Godunov-based method to the gaseous phase while using a flux corrected transport McCormack scheme for the particle phase. The experimental results presented by Zhang et al. [32] provide valuable insight into multiphase explosion phenomenology, and present a challenging benchmark for numerical model validation. Furthermore, the heuristic approach to developing a dispersed phase equation of state provides a powerful tool for representing the pressure of a collection of particles in the absence of a more rigorous theoretical approach, and is adopted in the current work. However, the application of such widely differing numerical methods to the individual phases is unattractive, and questions remain about the form of the governing equation for the particle phase, which no longer aligns with other models [1, 10, 25].

### 1.3 Statement of Work

The current work proposes, develops, and applies a compressible multiphase flow model for the study of multiphase explosions. Specifically, the model focuses on multiphase explosions containing a dispersed particle phase. The model development effort is motivated by the lack of a satisfactory model in the literature, and is intended to provide a computational tool for investigating fundamental aspects of multiphase explosions, which are important in many fields.

Two original contributions to the literature are made. The first is the development of a Godunov-based numerical technique for solving the multiphase flow equations. This technique is driven by a novel multiphase Riemann solver that is non-iterative and decoupled among phases. All phases are treated as compressible and full non-equilibrium among phases is allowed. Additionally, the numerical method allows for the proper representation of the mathematical characteristics of dispersed particle phases through the implicit assumption of a volume fraction

dependent equation of state. The second original contribution is the proposal and validation of a volume fraction dependent equation of state for dispersed materials. A generic equation of state format for representing the dependence of dispersed phase pressure on volume fraction is proposed and applied. Numerical calculations using this model are compared to experimental data, revealing the importance of accounting for the volume fraction effects, and validating the proposed model. This contribution is particularly important in the context of the disagreement over the representation of dispersed particle phases that exists in the literature.

The remainder of this document is organized as follows. In Ch. 2, the governing equations for compressible multiphase flows are derived and discussed. The derivation reveals the physical origins of individual terms in the governing equations, including the nozzling terms which are a source of debate in the literature. Following the derivation, both the nozzling terms and the nature of dispersed phase materials are discussed. The discussion of dispersed materials sets the stage for the dispersed phase equation of state that is later proposed, applied, and investigated. A brief review of the results of a characteristic analysis of the governing equations, which is included in the appendix, concludes this chapter.

Ch. 3 focuses on numerical model development. Here, the characteristic equations derived in the appendix are applied in the development of a multiphase Riemann solver. The multiphase Riemann solver forms the basis of a Godunov-based method for the numerical solution of the governing equations. Correlations for interphase drag and heat transfer are taken from the literature and presented. Finally, a generic equation of state for the representation of dispersed materials is proposed and discussed.

In Ch. 4, numerical calculations are performed and compared with existing experimental data. Simulations are based on the work of Zhang, et al. [32], as well as Carney and Lightstone [3]. Both cases involve the detonation of a

charge containing inert particles surrounded by an explosive fill. Results for shock and particle front motion, as well as range-dependent pressures agree well with experimental data, providing confidence in the numerical methods developed.

Finally, Ch. 5 and Ch. 6 focus on the effects modeling correlations and physical parameters have on the calculated solutions. Ch. 5 focuses specifically on the sensitivities of the model to correlations for drag, heat transfer, and dispersed phase pressure. Numerical results obtained with various correlations reveal the influence of the correlations on the solution, and indicate which modeling strategies compare best with experiment. Perhaps most importantly, a comparison of various representations of dispersed phase pressure reveal that accounting for volume fraction effects is critical to obtaining accurate solutions. This comparison also validates the physical description of dispersed materials that forms the basis of the proposed dispersed phase equation of state. Ch. 6 then focuses on the effect physical parameters have on the explosion dynamics. The parameters investigated include particle loading, size, and material. The results indicate the ability of these parameters to significantly modify the explosion dynamics. These results provide important fundamental information necessary for designing and analyzing systems that employ multiphase explosion technologies.

## Chapter 2

### Governing Equations

In this chapter, the governing equations for a compressible multiphase flow are derived and discussed. The derivation provides insight into the physical origins of the individual terms in the governing equations, including the nozzling terms, which can be difficult to discern from the literature. A discussion of the physical nature of dispersed materials follows the derivation. Proper modeling of dispersed phase materials is a distinguishing feature of this work. A detailed examination of the nozzling terms is then presented. Finally, the results of a characteristic analysis, the details of which are given in the appendix, are reviewed. This chapter provides both a mathematical model for, and physical insight into compressible multiphase flows. It provides the basis for understanding the numerical algorithms developed and numerical simulations performed throughout the remainder of this work.

#### 2.1 Derivation of Governing Equations

To begin the derivation, an Eulerian control volume containing multiple materials that are intermixed but occupy separate volumes is considered. Fig. 2.1 depicts such a scenario in which a collection of particles is dispersed in a continuous media. The control volume pictured is a one-dimensional non-uniform duct with

fixed total volume  $V$ , and fixed boundaries of areas  $A_1$  and  $A_2$  through which flow passes. The notion of a one-dimensional non-uniform duct is carried through the derivation, resulting in a one-dimensional set of governing equations that are later applied to systems of higher dimension using dimensional splitting [29, 15].

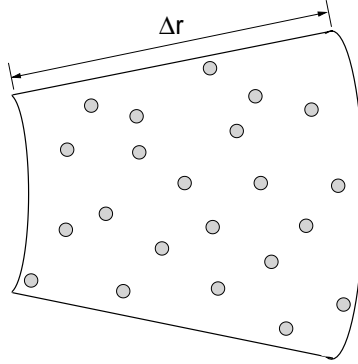


Figure 2.1: Eulerian control volume containing multiphase flow.

Each phase  $k$  in the flow retains a separate volume (defined by the volume fraction  $\alpha_k$ ), density  $\rho_k$ , velocity  $u_k$ , temperature  $T_k$ , pressure  $P_k$ , and energy  $E_k$ . Three assumptions that are standard in nearly all current compressible multiphase models [1, 10, 25] are applied. First, the area acted on by a phase  $k$  is assumed to be the volume fraction  $\alpha_k$  occupied by that phase multiplied by the total area, so that  $A_k = \alpha_k A$ . Second, each phase is assumed to move independently except during the interaction processes when volume, mass, momentum, and energy are exchanged. Third, dissipative effects are accounted for among phases, but assumed to be negligible within each phase.

### 2.1.1 Continuity Equation

The continuity equation expresses the conservation of mass for each phase. It states that the change in mass of a phase  $k$  in a control volume is equal to the net

mass flow in and out of the control volume plus the mass production. Expressing this in the context of Fig. 2.1 gives:

$$\Delta_t (\alpha_k V \rho_k) = (\alpha_k A \rho_k u_k) \Big|_1 - (\alpha_k A \rho_k u_k) \Big|_2 + \dot{m}_k V \quad (2.1)$$

Where  $\Delta_t$  represents the time derivative. Noting that the total volume  $V$  is constant, and expressing the net mass flow in terms of the difference operator  $\Delta () = ()_2 - ()_1$ , leads to the continuity equation:

$$V \Delta_t (\alpha_k \rho_k) + \Delta (\alpha_k \rho_k u_k A) = \dot{m}_k V \quad (2.2)$$

Mass conservation also requires that the summation of the mass exchanged among phases is zero:

$$\sum_k \dot{m}_k = 0 \quad (2.3)$$

### 2.1.2 Momentum Equation

The momentum equation states that the change in momentum in a control volume is equal to the net flow of momentum in and out of the control volume plus the momentum production and the sum of the forces acting on the volume. Equating the time rate of change of momentum, net momentum flow, and momentum production due to chemical reaction with the forces acting on the phase yields:

$$V \Delta_t (\alpha_k \rho_k u_k) + \Delta (\alpha_k \rho_k u_k^2 A) - \dot{m}_k u_R V = \sum F_k \quad (2.4)$$

Where  $u_R$  represents the velocity of the reacting phase, which is the phase from which mass is donated during reaction. The forces acting on each phase in the control volume include the pressure force, gravity force, and drag force. Summing

the pressure forces on a phase in the control volume gives:

$$F_{P,k} = P_k \alpha_k A \Big|_1 - P_k \alpha_k A \Big|_2 + P_{s,k} \Delta (\alpha_k A) \quad (2.5)$$

Where  $P_{s,k}$  is the average sidewall pressure acting on phase  $k$ . Simplifying this expression with the difference operator yields:

$$F_{P,k} = -\Delta (\alpha_k P_k A) + P_{s,k} \Delta (\alpha_k A) \quad (2.6)$$

The gravity force acting on the mass of a phase inside the control volume is:

$$F_{g,k} = \alpha_k \rho_k g V \quad (2.7)$$

The drag force acting on a phase may consist of both pressure drag and velocity drag, although many multiphase explosion models only include the velocity drag component [1, 32]. Crowe, et al. [4] provide a good discussion of the drag force. Because there are many expressions that can be applied, no specific form of the drag force is included here. Rather, the drag force is simply given as:

$$F_{d,k} = f_{d,k} V \quad (2.8)$$

Summing the forces yields:

$$\sum F_k = -\Delta (\alpha_k P_k A) + P_{s,k} \Delta (\alpha_k A) + \alpha_k \rho_k g V + f_{d,k} V \quad (2.9)$$

Substituting this into Eq. (2.4) then provides the momentum equation:

$$V \Delta_t (\alpha_k \rho_k u_k) + \Delta (\alpha_k \rho_k u_k^2 A + \alpha_k P_k A) = P_{s,k} \Delta (\alpha_k A) + \alpha_k \rho_k g V + f_{d,k} V + \dot{m}_k u_R V \quad (2.10)$$

### 2.1.3 Energy Equation

The energy equation is an expression of the first law of thermodynamics. It states that the change in total energy in a control volume is equal to the net energy flow through the volume plus the energy production and heat transferred to the system, and minus the work done by the system. The equation expressing this is:

$$V \Delta_t (\alpha_k \rho_k E_k) + \Delta (\alpha_k \rho_k u_k E_k A) - \dot{m}_k E_R V = \dot{Q} - \dot{W} \quad (2.11)$$

Where the total energy is defined as:

$$E_k = e_k + \frac{1}{2} u_k^2 \quad (2.12)$$

In Eq. (2.11),  $E_R$  is the total energy of the reacting phase, which is the phase from which mass is donated in a chemical reaction. Work terms affecting the system include flow work, gravitational work, drag work, and work due to volume change. The rate of flow work is expressed as:

$$\dot{W}_{f,k} = \Delta (\alpha_k u_k P_k A) \quad (2.13)$$

The rate of work due to gravity is:

$$\dot{W}_{g,k} = -\alpha_k \rho_k u_k g V \quad (2.14)$$

The rate of work from drag is:

$$\dot{W}_{d,k} = -u_D f_{d,k} V \quad (2.15)$$

The rate of work due to volume change is:

$$\dot{W}_{V,k} = P_i \dot{V}_k = P_i V \Delta_t \alpha_k \quad (2.16)$$

Here, the pressure relevant to the volume change work is termed the interfacial pressure  $P_i$ . The interfacial pressure must be equal among phases to ensure energy conservation; it cannot equal the phase pressure  $P_k$  for all phases. If the phase pressure  $P_k$  were applied in the volume change work, the energy change would be isentropic for all phases. This is not physically correct however since energy is not conserved along an isentrope.

Heat transfer occurs as the result of temperature non-equilibrium among phases. Many correlations for heat transfer are available. To preserve the generality of the governing equations, the rate of energy exchange due to heat transfer is expressed as:

$$\dot{Q}_k = \dot{q}_k V \quad (2.17)$$

Substituting Eqs. (2.13-2.17) into Eq. (2.11) yields the final form of the energy equation:

$$\begin{aligned} V \Delta_t (\alpha_k \rho_k E_k) + \Delta (\alpha_k u_k A [\rho_k E_k + P_k]) = \\ - P_i V \Delta_t (\alpha_k) + \dot{q}_k V + \alpha_k \rho_k u_k g V + u_D f_{d,k} V + \dot{m}_k E_R V \end{aligned} \quad (2.18)$$

### 2.1.4 Number Density Equation

For multiphase flow problems containing droplets or particles, it may be necessary to track the number density  $N_k$  of the dispersed phase. Number density, like mass density, is a conserved variable; it has units of (no. particles per total volume). Representing the the rate of fusion or break-up of particles by  $\dot{N}_k$ , the number density equation has the form:

$$V \Delta_t (N_k) + \Delta (N_k u_k A) = \dot{N}_k V \quad (2.19)$$

### 2.1.5 Convected Variable Equation

Many physical models contain variables that are convected with the flow. Examples include chemical species, burn fractions, or off-axis velocity terms. Representing any convected variable by  $v_{k,j}$ , and the volumetric mass production rate for species  $j$  of phase  $k$  by  $\dot{\omega}_{k,j}$ , the convected variable equation is:

$$V \Delta_t (\alpha_k \rho_k v_{k,j}) + \Delta (\alpha_k \rho_k v_{k,j} u_k A) = \dot{\omega}_{k,j} V \quad (2.20)$$

### 2.1.6 Volume Fraction Equation

In addition to those derived above, an additional relation governing the partitioning of volume among phases is needed to close the system of equations. Two options exist: 1) the assumption of pressure equilibrium among phases, and 2) the application of an evolutionary equation for volume fraction. Both choices present complications. If the first option is chosen, the volume fractions for each phase are fully defined at the pressure equilibrium state. However, the rigid application of pressure equilibrium can lead to ill-posed systems of equations [1, 8]. The second option is complicated by the fact that volume is not a conserved variable, making

it difficult to form an evolutionary equation. Despite this, most current methods for solving compressible multiphase flow problems [1, 10, 25, 32] do employ an evolutionary equation for volume fraction. Baer and Nunziato [1] proposed a dynamic compaction equation for tracking the evolution of volume fraction that has become somewhat standard. Saurel and Lemetayer [25] have written this equation in the slightly more general form shown below.

$$\frac{\partial \alpha_k}{\partial t} + u_i \frac{\partial \alpha_k}{\partial r} = \mu \left( P_{int,k} - P'_{int,k} \right) + \frac{\dot{m}_k}{\rho_R} \quad (2.21)$$

Where  $\mu$  is the compaction viscosity [1], and the expression  $\left( P_{int,k} - P'_{int,k} \right)$  denotes the change in pressure as the phases relax toward equilibrium [25]. This equation is written in a non-unique manner, but satisfies the physical notion that volume adjusts in conformance with convection, mass exchange, and pressure relaxation over time. It states that the volume fraction of each phase is convected along a streamline at the interfacial velocity  $u_i$ , and adjusts to pressure equilibrium with a timescale governed by  $\mu$ . The value of  $u_i$  is common among all phases, ensuring that all volume fractions sum to unity. While other evolutionary equations for volume fraction are certainly possible, the form shown in Eq. (2.21) is adopted in the current work.

## 2.2 Multiphase Equations in Differential Form

In section 2.1 the governing equations for a compressible multiphase flow were derived using a control volume analysis. However, it is instructive to put the governing equations in differential form. The differential form is the starting point for the characteristic analysis, which is used to determine the mathematical characteristics of the governing equations. It is also the most widely used form in the literature and thus necessary for comparing the current mathematical model with existing models. Additionally, the differential form derived here allows for the use of Cartesian (planar), cylindrical, or spherical coordinate systems, adding to the utility of the numerical model.

Determining the differential form of the governing equations requires the geometrical terms shown in Tab. 2.1. When comparing these terms with the control volume shown in Fig. 2.1, cell edge 1 is located at radial distance  $r$ , and edge 2 is located at radial distance  $r + \Delta r$ . The differential form of the governing equations is determined by substituting the edge areas and volumes into the derived equations. Because the differential form is sought, the volume is taken in the limit of  $\Delta r \rightarrow 0$ .

<i>Geometry</i>	<i>Area(r)</i>	<i>Volume</i>	<i>Volume <math>\Delta r \rightarrow 0</math></i>
Cartesian	$A = \text{constant}$	$A\Delta r$	$A\Delta r$
Cylindrical	$2\pi hr$	$\pi [(r + \Delta r)^2 - r^2] h$	$2\pi hr\Delta r$
Spherical	$4\pi r^2$	$(4/3)\pi [(r + \Delta r)^3 - r^3]$	$4\pi r^2\Delta r$

Table 2.1: Coordinate System Geometries

The resulting differential forms of the governing equations are given below. The equations are cast in Cartesian, cylindrical, or spherical coordinates by setting  $n = 0, 1, \text{ or } 2$ , respectively.

$$\frac{\partial (r^n \alpha_k \rho_k)}{\partial t} + \frac{\partial}{\partial r} (r^n \alpha_k \rho_k u_k) = r^n \dot{m}_k \quad (2.22)$$

$$\begin{aligned} \frac{\partial (r^n \alpha_k \rho_k u_k)}{\partial t} + \frac{\partial}{\partial r} (r^n \alpha_k \rho_k u_k^2 + r^n \alpha_k P_k) &= P_{s,k} \frac{\partial (r^n \alpha_k)}{\partial r} \\ &+ r^n \dot{m}_k u_R + r^n f_k + r^n \alpha_k \rho_k g \end{aligned} \quad (2.23)$$

$$\begin{aligned} \frac{\partial (r^n \alpha_k \rho_k E_k)}{\partial t} + \frac{\partial}{\partial r} (r^n \alpha_k u_k [\rho_k E_k + P_k]) &= r^n P_i u_i \frac{\partial \alpha_k}{\partial r} \\ &- r^n P_i \mu (P_{int,k} - P'_{int,k}) + r^n \dot{m}_k E_{kR} + r^n f_k u_D + r^n \alpha_k \rho_k u_k g \end{aligned} \quad (2.24)$$

$$\frac{\partial (r^n \alpha_k \rho_k v_{k,j})}{\partial t} + \frac{\partial}{\partial r} (r^n \alpha_k \rho_k v_{k,j} u_k) = r^n \dot{\omega}_{k,j} \quad (2.25)$$

$$\frac{\partial (r^n N_k)}{\partial t} + \frac{\partial}{\partial r} (r^n N_k u_k) = r^n \dot{N}_k \quad (2.26)$$

$$\frac{\partial \alpha_k}{\partial t} + u_i \frac{\partial \alpha_k}{\partial r} = \mu (P_{int,k} - P'_{int,k}) + \frac{\dot{m}_k}{\rho_R} \quad (2.27)$$

## 2.3 Discussion

While Eqs. (2.22-2.26) have been derived independently, they agree well with the others presented in the literature [1, 10, 25]. When comparing the set of equations presented above with others in the literature, the reader will find that the form of the nozzling terms has been generalized in the current mathematical model. The physical motivation behind this generalization is discussed in this section. Preceding this, another topic important to the closure of the system of equations is addressed: the modeling of dispersed phase materials. Here, the

physical nature of dispersed phase materials is discussed, and the functional form of the equation of state (EOS) required to model these materials is presented.

### 2.3.1 Dispersed Phase Material Modeling

The treatment of dispersed phases is critical in modeling multiphase explosions and is the area wherein most discrepancies among modeling approaches exist. Dispersed phases are defined as those whose constituent material is not physically connected [4]. Such is the case when modeling a collection of particles where the particle size is smaller than the size of the computational grid. While the material within an individual particle is physically connected, the particles themselves are not. The lack of physical connection in a dispersed phase creates material properties for the collection of particles that are quite different from the properties of a continuous (non-dispersed) material. It is important to recognize that when discussing a dispersed-phase material, two distinct pressures exist. The first is the pressure existing within the individual particles making up the phase. The second is the pressure exerted by the collection of particles. For the purposes of the current work, the former will be given the distinction of being referred to as the *internal pressure*  $P_{int}$ , while the latter will be referred to as the *phase pressure* or simply the *pressure*  $P$ . Considering any individual particle in a dispersed phase, it is clear that the material making up that particle is physically connected; therefore, as with any continuous (non-dispersed) material, the internal pressure for a dispersed phase is found using an equation of state of the form  $P_{int} = P_{int}(\rho, e)$  or  $P_{int} = P_{int}(\rho, T)$ . Conversely, the particles whose collection makes up a dispersed phase are not physically connected. In this case, the pressure of the phase exists due to direct particle interactions through contact or collisions [4, 8, 32]. Because direct particle contact and the probability of particle collisions are strongly tied to particle spacing, volume fraction is a key variable in determining the pressure of a

dispersed phase.

To enable the modeling of multiphase flows containing a dispersed particle phase, the functional form of the equation of state must be addressed. Following the work of Zhang et al. [32], a generic equation of state with a functional dependence on volume fraction is assumed. The pressure of any phase is therefore represented as:

$$P_k = P_k(\alpha_k, \rho_k, e_k) \quad (2.28)$$

This expression is general and applies equally well to either a dispersed or continuous phase, where in the case of a continuous phase the functional dependence on volume fraction is null. The internal pressure of a phase, which does not depend on volume fraction, is represented in the typical fashion:

$$P_{int,k} = P_{int,k}(\rho_k, e_k) \quad (2.29)$$

Again, the distinction between pressure and internal pressure is necessary when discussing flows containing dispersed phases. For a continuous phase no distinction exists, such that  $P_C = P_{int,C}$ .

While the functional dependence of the dispersed phase pressure on particle volume fraction has certainly been recognized in the literature [4, 8, 32], this dependence is not discussed or applied in many influential works relating to multiphase explosions [1, 10, 25, 2, 13]. Instead, these models assume that the pressure of the dispersed phase is equal to the internal pressure within the particles so that  $P_k = P_{int,k}$ . In the case of mathematical models focused exclusively on DDT [1, 10, 2, 13], this assumption may be justifiable because the particle flows are largely granular and heavily confined. However, as the particle volume fraction drops this assumption is not longer physically accurate. Accounting for the func-

tional dependence of pressure on volume fraction is a distinguishing feature of the current mathematical model.

### 2.3.2 Discussion of Nozzling Terms

The nozzling terms are the first terms on the right hand side of the momentum (2.23) and energy (2.24) equations. These terms are a source of debate in the literature; they are included by some authors [1, 25], and excluded by others [10, 17]. When included, the forms of the nozzling terms are slightly different than those shown in Eqs. (2.23) and (2.24). In the momentum equation, the form typically shown in the literature is:

$$P_i \frac{\partial \alpha_k}{\partial r} \tag{2.30}$$

While the form typically shown in the energy equation is:

$$P_i u_i \frac{\partial \alpha_k}{\partial r} \tag{2.31}$$

The radius term  $r^n$  shown in the current mathematical model does not appear in the typical forms of the equations because these are cast in purely Cartesian (planar) coordinates, allowing this term to cancel out. The more notable difference between the typical and current forms of the nozzling terms exists in the value of the pressures that pre-multiply the derivatives in each equation. In the literature, the interfacial pressure  $P_i$  is applied in both the momentum and energy equations, while in the current model separate values are applied in each equation. In the momentum equation (2.23), the value of pressure pre-multiplying the derivative is the sidewall pressure  $P_{s,k}$ , which is allowed to vary among phases. In the energy equation (2.24), the interfacial pressure  $P_i$  is applied. Hence, the form of the energy

equation nozzling term is equivalent to that typically presented in the literature, while the form of the momentum equation nozzling term is not.

To understand the reason for this discrepancy, one must consider the physical origin of the nozzling term in the momentum equation (2.23). From Sec. 2.1.2, the nozzling term arises from the force acting on the sidewalls of a non-uniform duct. This force is well-established in the derivation of the Euler equations. In the case of the Euler equations, the sidewall force has the form  $P_s \Delta A$ , while in multiphase flows it is taken as  $P_{s,k} \Delta (\alpha_k A)$  for a given phase  $k$ . The challenge then becomes defining the sidewall pressure. For the Euler equations the choice is clear: the sidewall pressure is simply the average cell pressure so that  $P_s = P$ . However, this choice is not as obvious for multiphase flows. In this case, dispersed phases have two distinct pressures: the phase pressure  $P_k$  and the internal pressure  $P_{int,k}$ . Given the physical meaning of the sidewall force, the the proper choice for the sidewall pressure would appear to be the phase pressure so that  $P_{s,k} = P_k$ . Obviously, this does not align with the typical definition of the momentum equation nozzling term, where  $P_{s,k} = P_i$ . To investigate the ramifications of these two choices, consider the following summations of the pressure terms in the momentum equation under each approach.

$$\begin{aligned} \text{Case 1: } P_{s,k} &= P_k \\ \frac{\partial}{\partial r} (r^n \alpha_k P_k) - P_k \frac{\partial}{\partial r} (r^n \alpha_k) &= r^n \alpha_k \frac{\partial P_k}{\partial r} \end{aligned} \quad (2.32)$$

$$\begin{aligned} \text{Case 2: } P_{s,k} &= P_i \\ \frac{\partial}{\partial r} (r^n \alpha_k P_k) - P_i \frac{\partial}{\partial r} (r^n \alpha_k) &= r^n \alpha_k \frac{\partial P_k}{\partial r} - (P_i - P_k) \frac{\partial}{\partial r} (r^n \alpha_k) \end{aligned} \quad (2.33)$$

From Eq. (2.32) the case in which  $P_{s,k} = P_k$  simplifies to a result in which a pressure gradient is necessary to accelerate the flow. In this case, as in the Euler equations, a change in area alone does not result in a force on the fluid. Conversely, from Eq. (2.33) if  $P_{s,k} = P_i$  a net force is exerted on the flow even in the absence of a pressure gradient if a change in area or volume fraction exists. This is true except in the special case where  $P_k = P_i$ ; however, since only the internal pressures, and not the phase pressures are driven toward equilibrium, this exception will rarely occur. Hence in this case, an initially stationary flow in a duct of varying physical area or volume fraction would be spontaneously accelerated even in the absence of a pressure gradient.

While the form of the momentum equation nozzling term in which  $P_{s,k} = P_i$  is typical of works including the nozzling terms in the literature [1, 25], it is not clear that this is the appropriate choice. First, as shown above, this choice can result in a force being exerted on the flow even in the absence of a pressure gradient. Additionally, the works proposing this form of the governing equations [1, 25] do not account for the dual-pressure nature of dispersed phases. Because these models assume  $P_k = P_{int,k}$  the pressures of each phase will tend toward equilibrium, making  $P_k \approx P_i$ , and negating the artificial acceleration discussed above. Hence this affect may be fortuitously avoided in such models. On the other hand, setting  $P_{s,k} = P_i$  ensures that the governing equations obey the strong form of the second law of thermodynamics [1]. As this discussion makes clear, significant debate surrounds the nozzling terms. Given this, it is desirable to derive a model and numerical method that are general enough to represent multiple forms of these terms. In Eqs. (2.23) and (2.24) the expressions for the nozzling terms are sufficiently general such that any relevant formulation can be obtained by altering the values of  $P_{s,k}$  and  $P_i$ . Two possibilities exist. First, setting  $P_{s,k} = P_k$  in Eq. (2.23) and  $P_i = 0$  in the energy equation (2.24) nozzling term eliminates

the traditional form of the nozzling terms while retaining the sidewall pressure necessary when considering flow in a geometrically non-uniform duct. Second, setting  $P_{k,s} = P_i$  in Eq. (2.23) while leaving Eq. (2.24) unmodified produces the traditional form of the nozzling terms. This generalization is carried throughout the numerical algorithm development to ensure the applicability of the derived modeling techniques to all forms of the governing equations.

## 2.4 Results of Characteristic Analysis

A characteristic analysis of the governing equations (2.22–2.27) has been performed. The details of this analysis, including the derivation of the characteristic relations, are included in the appendix. By re-writing the governing equations in terms of primitive variables, and assuming a general equation of state of the form given in Eq. (2.28), the eigenvalues, eigenvectors, and characteristic equations of the compressible multiphase flow equations were derived. The system of equations is hyperbolic, having real eigenvalues and distinct eigenvectors. The eigenvalues show that four characteristic speeds exist:

$$\lambda_i = u_i; \quad \lambda_0 = u_k; \quad \lambda_+ = u_k + c_k; \quad \lambda_- = u_k - c_k \quad (2.34)$$

The definition of  $c_k$  comes directly from the characteristic analysis, and follows from:

$$c_k^2 = \left. \frac{\partial P_k}{\partial \rho_k} \right|_{e,\alpha} + \frac{P_k}{\rho_k^2} \left. \frac{\partial P_k}{\partial e_k} \right|_{\rho,\alpha} = \left. \frac{\partial P_k}{\partial \rho_k} \right|_{s,\alpha} \quad (2.35)$$

This definition is of interest given the functional dependence of pressure on volume fraction that was assumed. From Eq. (2.35), the definition of  $c_k$  is observed to align with the standard definition of sound speed under the additional constraint of constant volume fraction.

Given the definition of sound speed and the eigenvalues, the multiphase equations are observed to possess the same characteristic velocities as the Euler equations, plus one additional characteristic velocity  $u_i$ . This interfacial velocity is the characteristic speed of the volume fraction discontinuity, following from Eq. (2.27). Understanding the mathematical characteristics of the governing equations is crucial for developing an accurate, stable, and consistent solution methodology. In the next chapter, results from the characteristic analysis are directly applied in the derivation of a numerical solution for the multiphase equations.

## Chapter 3

### Numerical Model Development

The numerical model developed is based on a purely Eulerian framework in which both continuous and dispersed phases are solved on a fixed grid. Within this framework, the governing equations are solved using a time- and dimensionally-split finite volume method. Using dimensional splitting, a one-dimensional solver is extended to perform simulations in one, two, or three spatial dimensions [29, 15]. Under the time-splitting approach, the governing equations are divided into convective terms and source terms that are solved independently within a single time-step [29, 15]. The convective step is solved using a Godunov-based method driven by a multiphase Riemann solver, while the source terms can be evaluated with any applicable ordinary differential equation (ODE) solver. The time-splitting approach to solving the multiphase flow equations has been applied successfully in the work of Saurel and Lemetayer [25]. A first-order splitting scheme is given below, where  $\mathbf{Q}$  is the solution vector,  $L_S$  is the source term operator and  $L_C$  is the convective operator; higher order schemes such as that of Strang [27] can also be applied.

$$\mathbf{Q}^{t+\Delta t} = L_S^{\Delta t} L_C^{\Delta t} \mathbf{Q}^t \quad (3.1)$$

### 3.1 Convective Operator Solution

Under the splitting procedure, the convective portion of the governing equations consist of all terms on the left hand side of Eqs. (2.22–2.27), plus the first term on the right hand side of Eqs. (2.23) and (2.24). All other terms on the right hand side of the equations are treated as source terms and excluded from the convective step. The solution of the equations will be discussed in a first-order, one-dimensional framework. Extension to higher order accuracy can be achieved by a number of methods already presented in the literature, and dimensional splitting can be used to solve problems in two or three dimensions [29, 15]. Applying a first-order finite volume method [29, 15] to the convective step results in the following numerical solution to the governing equations:

$$\mathbf{Q}_i^{t+\Delta t} = \mathbf{Q}_i^t - \frac{\Delta t}{\Delta r} [\mathbf{F}_{i+1/2}^t - \mathbf{F}_{i-1/2}^t - \phi (\mathbf{H}_{i+1/2}^t - \mathbf{H}_{i-1/2}^t)] \quad (3.2)$$

$$\mathbf{Q} = [\alpha_k, r^n \alpha_k \rho_k, r^n \alpha_k \rho_k u_k, r^n \alpha_k \rho_k E_k, r^n \alpha_k \rho_k v_{k,j}, r^n N_k]^T \quad (3.3)$$

$$\mathbf{F} = [0, r^n \alpha_k \rho_k u_k, r^n \alpha_k (\rho_k u_k^2 + P_k), r^n \alpha_k u_k (\rho_k E_k + P_k), r^n \alpha_k \rho_k v_{k,j} u_k, r^n N_k u_k]^T \quad (3.4)$$

$$\phi = \text{diag} [u_i, 0, P_{s,k}, -r_n P_i u_i, 0, 0] \quad (3.5)$$

$$\mathbf{H} = [\alpha_k, 0, r^n \alpha_k, \alpha_k, 0, 0]^T \quad (3.6)$$

To solve the convective portion of the governing equations, a Godunov-based method is applied. Here, the cell edge state used to calculate the intercell fluxes, which is referred to as the Godunov state, is determined through the solution of a Riemann problem with the right and left edge states as initial conditions [9]. In a first order method the right and left edge states are those of the adjacent cell

centers. The key to developing a successful method lies in determining an accurate and robust Riemann solver to predict the Godunov state and form the fluxes to solve Eq. (3.2).

The Riemann structure for the multiphase equations consists of four waves for any single phase. The characteristic velocities of these waves are those given in Eq.(2.34). Three of these waves align with those in the Euler equations, with the leading and trailing waves being shocks or expansions, and the intermediate wave being a contact discontinuity. The fourth wave is the volume fraction discontinuity which is convected with the interfacial velocity  $u_i$ . The interfacial velocity is assigned different values by different researchers [1, 25]; however, the value assigned should be bounded by the local fluid velocity of each phase. Hence for a two-phase flow:

$$u_i = u_i(u_1^*, u_2^*); \quad \text{where: } u_1^* \leq u_i \leq u_2^*, \text{ or } u_2^* \leq u_i \leq u_1^* \quad (3.7)$$

The value of the interfacial velocity is common among all phases, but depending on the definition applied does not necessarily coincide with the characteristic velocity of the other waves for any phase. Hence a generic solution to the multiphase Riemann problem consists of five states separated by four waves for any given phase. A generic wave structure for a two-phase flow is given in Fig. 3.1. Here,  $u_i$  is the interfacial velocity,  $u_k^*$  is the slip-line velocity for phase  $k$ , and the variables  $U_{(I,O),k}^{(L,R)}$  represent the speeds of either shocks or expansions in phase  $k$ . The superscripts  $L, R$  denote left or right running waves, and the subscripts  $I, O$  denote the inner and outer wave-speeds. In the case of a shock,  $U_I = U_O$ .

The solution of the multiphase Riemann problem is complicated by the presence of the volume fraction discontinuity, not only because a fourth wave exists for every phase, but also because the interfacial velocity is not known a priori. Moreover, because the interfacial velocity can be a function of all the phase velocities,

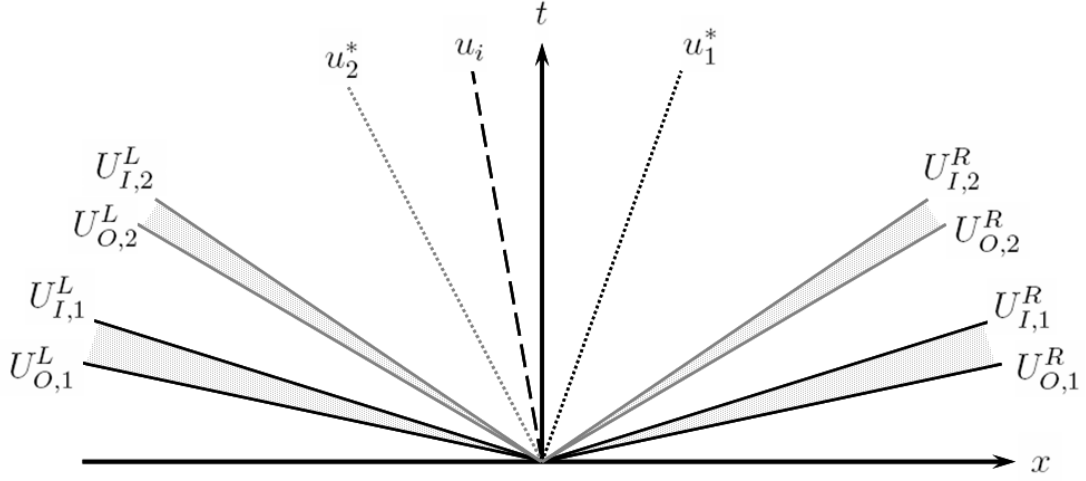


Figure 3.1: Generic Riemann structure for two-phase flow.

it is possible for the volume fraction discontinuity to lie within any region of the flow with respect to a single phase. Six scenarios for the location of the volume fraction discontinuity within any single phase exist. These scenarios are depicted in Fig. 3.2.

The Riemann problem, by definition, is constructed in Cartesian coordinates and does not contain source terms. An exact solution, even in the case of the Euler equations, requires iterative methods. As an alternative, a linearized solution can be found using the characteristic equations. The characteristic equations for a multiphase flow are derived in the appendix, and the characteristic equations for the Riemann problem are found by setting  $n = 0$  in Eqs. (A.14–A.19).

Constructing a linearized Riemann solution for the multiphase equations is complicated by the presence of the volume fraction discontinuity. For each phase, six separate solutions exist corresponding to the six possible locations of the volume fraction discontinuity shown in Fig 3.2. Moreover, the interfacial velocity is a function of the slip line velocities for each phase and is not known at the start of the Riemann problem solution. Because of this, the wave structure of the solution

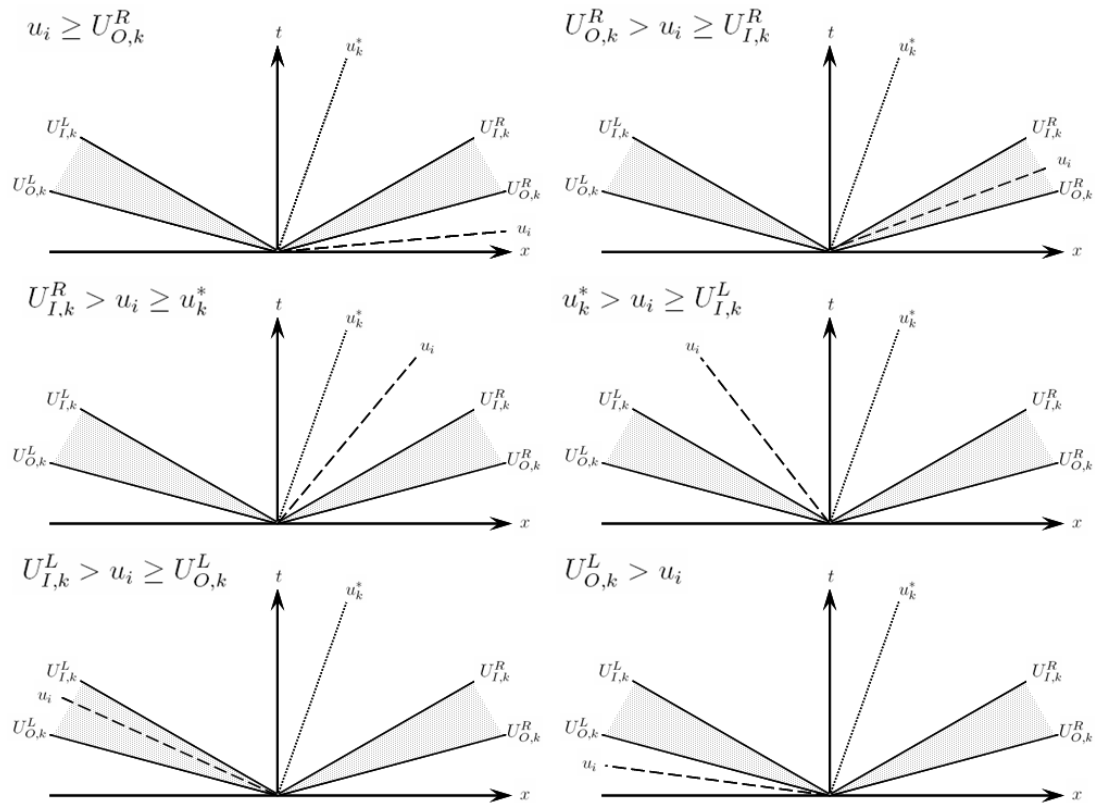


Figure 3.2: Possible locations of the volume fraction discontinuity within the Riemann structure for any given phase.

cannot be determined a priori; this necessitates an iterative approach in which a wave structure is guessed and the resulting solution checked for consistency with the assumed structure. This is an unattractive approach for use in a numerical model given the possibility of solving the Riemann problem six times at every cell boundary.

Closing the linearized solution presents another problem. The characteristic equations themselves are not sufficient to close the system of equations, and must be augmented with another relation for each phase. In the case of the Euler equations, the isentropic condition, which is valid along a streamline, is an obvious choice. However, this equation is not strictly applicable across the volume fraction discontinuity because flow is non-isentropic across this jump. Alternate relations based on a chain rule expansion of pressure can be derived, but solving the resulting system will be problematic because of the lack of a defined thermodynamic path.

To avoid the difficulties discussed above, two simplifications to the solver formulation are proposed. These simplifications are aimed at producing a robust, non-iterative, approximate Riemann solver for the multiphase equations. To form the solution, the following assumptions are made locally for each phase:

$$u_i = u_k; \quad P_i = P_{s,k} = P_k \quad (3.8)$$

The equilibration of the interfacial and phase velocities results in the alignment of the contact and volume fraction discontinuities. This decouples the solution among phases and removes the need for an iterative solution to find the proper wave structure. It also allows for the application of the isentropic condition along a streamline, since this path will not cross the volume fraction discontinuity. Assigning all pressures the value of the phase pressure simplifies the characteristic equations, which accordingly simplify the solution. Under these conditions, the characteristic

equations for each phase are reduced from those shown in Eqs. (A.14–A.19) to Eqs. (3.9–3.14) (now including the isentropic condition). The Riemann structure based on the simplified characteristic equations is shown in Fig. 3.3.

$$\lambda_0 = u_k : \quad d\alpha_k = 0 \quad (3.9)$$

$$dv_k = 0 \quad (3.10)$$

$$dN_k - \frac{N_k}{\alpha_k} d\alpha_k - \frac{N_k}{\rho_k h_k} d(\rho_k e_k) = 0 \quad (3.11)$$

$$d(\rho_k e_k) - \frac{\rho_k h_k (a_k^2 - c_k^2)}{\alpha_k c_k^2} d\alpha_k - \frac{h_k}{c_k^2} dP_k = 0 \quad (3.12)$$

$$dP_k - c_k^2 d\rho_k = 0 \quad (3.13)$$

$$\lambda_+ = u_k + c_k : \quad dP_k + \rho_k c_k du_k = 0 \quad (3.14)$$

$$\lambda_- = u_k - c_k : \quad dP_k - \rho_k c_k du_k = 0 \quad (3.15)$$

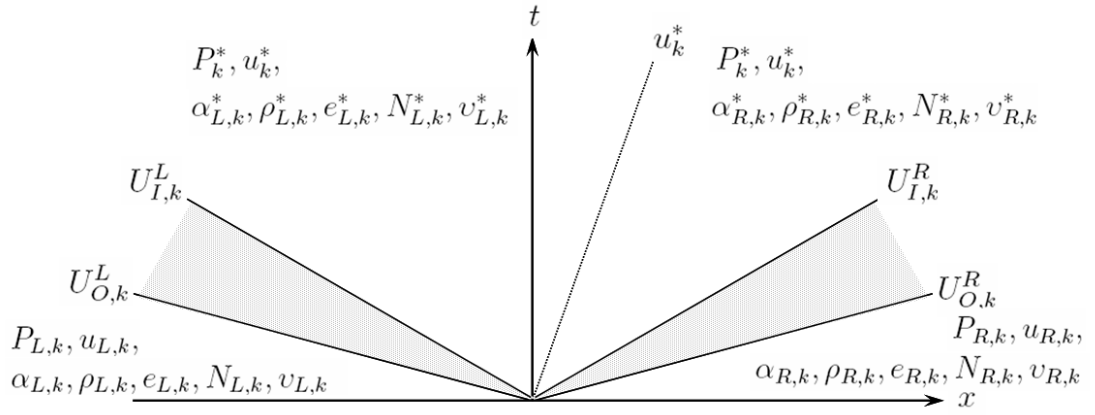


Figure 3.3: Structure of approximate Riemann solution for any single phase.

From Eqs. (3.9–3.14), an approximate Riemann solution can be derived by integrating along characteristics. Given the right and left states as initial conditions, the approximate solution is given by:

$$u_k^* = \frac{P_{L,k} - P_{R,k} + \rho_{L,k}c_{L,k}u_{L,k} + \rho_{R,k}c_{R,k}u_{R,k}}{\rho_{L,k}c_{L,k} + \rho_{R,k}c_{R,k}} \quad (3.16)$$

$$P_k^* = \frac{\rho_{R,k}c_{R,k}P_{L,k} + \rho_{L,k}c_{L,k}P_{R,k} + \rho_{L,k}c_{L,k}\rho_{R,k}c_{R,k}(u_{L,k} - u_{R,k})}{\rho_{L,k}c_{L,k}\rho_{R,k}c_{R,k}} \quad (3.17)$$

$$\text{for } S = L, R: \quad \alpha_{S,k}^* = \alpha_{S,k} \quad (3.18)$$

$$v_{S,k}^* = v_{S,k} \quad (3.19)$$

$$\rho_{S,k}^* = \rho_{S,k} - \frac{1}{c_{S,k}^2} (P_{S,k} - P_k^*) \quad (3.20)$$

$$e_{S,k}^* = \frac{1}{\rho_{S,k}^*} \left( \rho_{S,k}e_{S,k} - \frac{h_{S,k}}{c_{S,k}^2} (P_{S,k} - P_k^*) \right) \quad (3.21)$$

$$N_{S,k}^* = N_{S,k} - \frac{N_{S,k}}{\rho_{S,k}h_{S,k}} (\rho_{S,k}e_{S,k} - \rho_{S,k}^*e_{S,k}^*) \quad (3.22)$$

It is immediately observed that this solution is closely related to the three-wave primitive variable Riemann solver for the Euler equations presented in previous works [29, 30]. This solution is attractive because it is independent of any specific equation of state. It is applicable to any material as long as the pressure and sound speed can be determined as functions of the other state variables.

Of major importance in the numerical modeling of multiphase explosions is accurately treating the mathematical characteristics of a dispersed particle phase. Unlike continuous materials, the pressure and sound speed of a dispersed material become zero as the flow becomes sufficiently dilute. In this case, the mathematical

characteristics of the phase become hyperbolically degenerate [17], and the linearized Riemann solution becomes singular. When this happens, the eigenvalues of the phase collapse from  $u_k - c_k$ ,  $u_k$ , and  $u_k + c_k$  to simply  $u_k$ . The characteristics are now those of the inviscid Burger's equation, for which an exact Riemann solution is easily determined. The two possible structures of the Riemann solution are shown in Fig. 3.4. Toro [29] presents an excellent discussion of the Riemann solution for the inviscid Burger's equation that will not be repeated here. However, because the linearized Riemann solution presented in Eqs. (3.16–3.22) is decoupled among phases, the exact Burger's solution is easily substituted for a dispersed phase with zero sound speed.

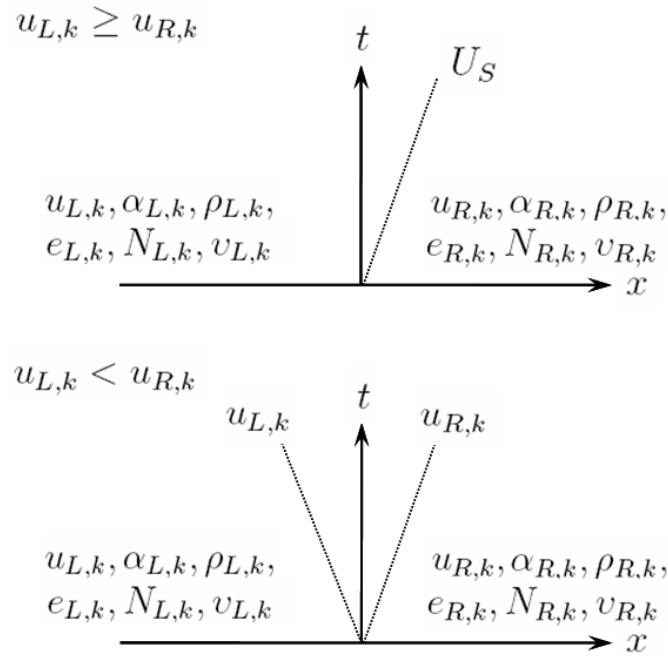


Figure 3.4: Structure of Riemann solution for hyperbolically degenerate systems.

The assumption of the local alignment of the phase and interfacial velocities for each phase in the Riemann problem decouples the solution among phases and leads to the derivation of a non-iterative solver. However, an inconsistency develops

under conditions in which the phase velocities are not equal. Specifically, the region of the multiphase Riemann solution between the contact discontinuities contains volume fractions that do not sum to one. This is not physically possible and requires correction.

To address this issue, consider the structure of the multiphase Riemann problem as shown in Fig. 3.5. The inconsistency in volume fractions occurs in the region between the contact discontinuities, which for the remainder of this discussion is termed the intermediate state. Since the numerical method being developed will be solved on a fixed grid, only the state along the vertical axis is relevant to the inter-cell fluxes. This means that the Riemann solver is self-consistent in an unmodified form in all cases except under states of flow reversal when the slip-line velocities are pointed in opposite directions. Multiple methods can be used to remedy this problem under states of flow reversal. Such methods include: averaging the right and left volume-fraction states for application in the intermediate state, or directly enforcing an interfacial velocity over which the volume fractions jump. The former approach is akin to smearing the volume-fraction discontinuity over the intermediate state, while the latter directly enforces the dynamic compaction equation (2.27). The latter approach is applied in the current work, with the interfacial velocity being set as that of the least compressible phase, which is the dispersed phase for all work completed to date. This choice of interfacial velocities aligns with the original definition of Bear and Nunziato [1].

Eqs. (3.16–3.22), in combination with the volume-fraction fix, produce an approximate Riemann solver for the multiphase equations. The solver is non-iterative and closely related to the primitive variable Riemann solver for the Euler equations presented in previous works [29, 30]. It is also independent of any specific equation of state format, making it applicable to many different material models. The cell-edge conditions are found by applying the approximate Riemann solution

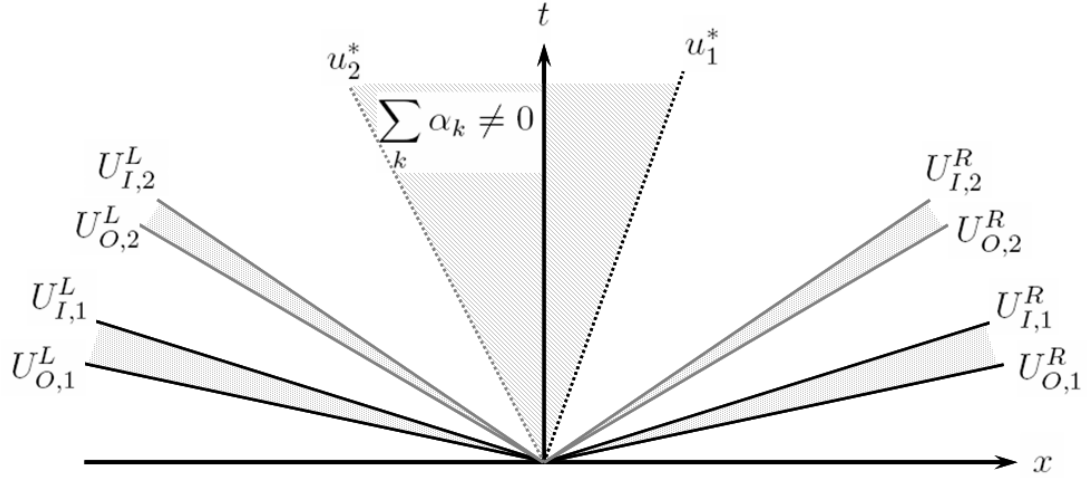


Figure 3.5: Structure of approximate Riemann solution for a two-phase flow before volume fraction inconsistency fix.

to the right and left states adjacent to the cell edge and sampling the solution along the edge. The flux terms are then formed by directly applying the cell edge states in Eq. (3.2).

### 3.2 Source Term Operator Solution

Source terms in the governing equations (2.22–2.27) are not included in the convective solution. These terms represent the exchange of volume, mass (or species), momentum, and energy among phases, as well as the effects of body forces such as gravity. Source terms typically do not contain derivatives and can be advanced in time using standard methods for solving ordinary differential equations, which will not be discussed here. However, it is important to focus on the specific models for drag, heat transfer, and pressure relaxation that determine the form of the source terms in the current study. All numerical simulations presented in this paper use inert particles, so rate laws for reacting particles – which can be

quite complex and highly dependent on the specific materials that are reacting – are not employed here.

A common method of expressing the drag force occurring due to velocity non-equilibrium between a particle and the surrounding media is to use the correlation shown below. The drag force  $f$  is expressed as a function of the drag coefficient  $C_D$ , which in this case is taken from Rowe [22].

$$f = 3\pi D\mu_C C_d (u_C - u_D) N \quad (3.23)$$

$$C_d = \begin{cases} 1 + 0.15 Re_R^{0.687} & \text{if } Re_R < 1000 \\ 0.01833 Re_R & \text{if } Re_R \geq 1000 \end{cases} \quad (3.24)$$

$$Re_R = \frac{\rho_C D |u_C - u_D|}{\mu_c} \quad (3.25)$$

This correlation is based on low Mach number flow over an isolated sphere, and may be expected to provide reasonable results in situations where these assumptions are valid. Papalexandris [17] applied this expression in studies of multiphase detonations involving dilute collections of particles. In many multiphase explosive applications however, the Mach number and particle volume fraction can be sufficiently high that these assumptions are no longer valid. To model the drag at increased Mach numbers, Tedeschi et al. [28] propose multiplying the base drag force in Eq. (3.23) by:

$$C_M = \begin{cases} 1 & \text{if } M < 0.3 \\ 1 + \frac{Re_R^2}{Re_R^2 + 100} e^{-0.225/M^{2.5}} & \text{if } M \geq 0.3 \end{cases} \quad (3.26)$$

To account for the effects of volume fraction, numerous researchers [21, 31, 6] have proposed corrections to Eq. (3.23). Here, the advice of Crowe et al. [4] is followed

and the correction of Wen and Yu [31] is chosen. This correction multiplies the base drag force (3.23) by  $\alpha_C^{-3.7}$ . Applying both this and the Mach number correction (3.26) results in the following expression for the drag force:

$$f = \alpha_C^{-3.7} 3\pi D \mu_C C_d C_M (u_C - u_D) N \quad (3.27)$$

In the case of sufficiently dense particle flows even the volume fraction correction applied in Eq. (3.27) may be insufficient to model the increased drag force [4]. Because of this, Crowe et al. [4] recommend the use of an alternate expression when  $\alpha_D \geq 0.2$ . Under these conditions Eq. (3.27) is replaced by the correlation of Shepherd and Begeal [26]:

$$f = \frac{33\mu_C}{D^2\alpha_C^{4.5}} \left( 1 + 0.01 Re_R \frac{\alpha_C}{\alpha_D} \right) (u_C - u_D) \quad (3.28)$$

Convective heat transfer between the particles and surrounding media is modeled using the correlation:

$$\dot{q} = \pi D \lambda_C Nu (T_C - T_D) N \quad (3.29)$$

The heat transfer is a function of the temperature difference and Nusselt number  $Nu$ . The Nusselt number is modeled as a function of the relative Reynolds number  $Re_R$  and Prandtl number  $Pr$  using the correlation of Ranz and Marshall [19, 20]:

$$Nu = 2 + 0.6 Re_R^{0.5} Pr^{0.33} \quad (3.30)$$

The term  $\mu (P_{int,k} - P'_{int,k})$  in Eq. (2.27) represents the volume change as phases relax toward pressure equilibrium. Modeling this process requires a correlation or estimate for the compaction viscosity  $\mu$ , which controls the rate

of relaxation. Physically, the rate at which phases relax to pressure equilibrium depends both on the compressibility of the materials and on the topology of the flow [25]. However, to date no formal, validated methodology for calculating  $\mu$  exists.

Difficulties in obtaining a value for the compaction viscosity can be circumvented by assuming it to be infinite. This allows all phases to relax to full pressure equilibrium during the source term solution in each time-step. The assumption of an infinite compaction viscosity is justifiable in a numerical model if the time-scale for pressure equilibration is smaller than the computational time-step. In an explicit model, the time-step is governed by the well-known CFL condition, and is proportional to the time for a wave to cross a computational cell. The timescale for a particle to relax to equilibrium with its surroundings is proportional to the time for a wave to propagate through the particle. The ratio of the computational time step and the relaxation timescale can be approximated by:

$$\frac{\tau_{comp}}{\tau_{relax}} \approx \frac{\Delta r}{c_{k,max}} \frac{c_{int,D}}{D} \quad (3.31)$$

Here,  $\Delta r$  and  $D$  are the computational cell size and particle diameter, respectively, and  $c_{k,max}$  and  $c_{D,int}$ , are the maximum sound speed in any phase, and internal sound speed in a particle, respectively. To model a collection of particles as a continuum, the particle size is required to be much smaller than the computational cell size; hence  $\Delta r \gg D$ . Additionally, the maximum sound speed in any phase must be greater than or equal to the sound speed within a particle, such that in the worst case  $c_{k,max} = c_{D,int}$ . This implies  $\tau_{comp} \gg \tau_{relax}$ , satisfying the requirements for assuming an infinite compaction viscosity. Given this, the compaction viscosity  $\mu$  is taken as infinite in the current work. However, this is not a requirement of the model or numerical methods, and a finite rate can be used if desired.

### 3.3 Dispersed Phase Equation of State

To close the numerical model, an equation of state properly modeling the dependence of the dispersed phase pressure on volume fraction  $\alpha_D$  is needed. Representing the pressure of a collection of particles in shock loading scenarios from a first-principals approach is a daunting task and has not yet been sufficiently addressed in the literature. In the absence of a more rigorous approach, Zhang et al. [32] have proposed using a heuristic interpolation method to define a dispersed phase equation of state. The basic principals of the heuristic approach of Zhang et al. [32] are adopted in this work to define a dispersed phase equation of state for the current model.

Fundamentally, the heuristic method of determining an equation of state for a dispersed particle phase states that two limits can be defined at which the pressure of the dispersed phase  $P_D$  will be known: 1) the dilute flow limit, which occurs when  $\alpha_D$  is sufficiently low such that the pressure of the collection of particles is taken as zero, and 2) the dense limit, occurring when  $\alpha_D$  is sufficiently high that the pressure exerted in the particle phase is equal to that of the pure material at the corresponding thermodynamic state. These limits place the following boundary conditions on the dispersed phase equation of state, which has a functional form defined by Eq. (2.28):

$$P_D(\alpha_{min}, \rho_D, e_D) = 0 \tag{3.32}$$

$$P_D(\alpha_{max}, \rho_D, e_D) = P_{int,D}(\rho_D, e_D) \tag{3.33}$$

If these two limits are known, the challenge is then to define the pressure in the transition regime between them. To satisfy the requirements imposed on the dispersed phase equation of state (2.28,3.32,3.33) a piecewise definition of the follow-

ing form is proposed:

$$P_D = \zeta(\alpha_D) P_{int,D}(\rho_D, e_D);$$

$$\zeta(\alpha_D) = \begin{cases} 0 & \text{if } \alpha_D \leq \alpha_{min} \\ \left(\frac{\alpha_D - \alpha_{min}}{\alpha_{max} - \alpha_{min}}\right)^z & \text{if } \alpha_{min} < \alpha_D < \alpha_{max} \\ 1 & \text{if } \alpha_{max} \leq \alpha_D \end{cases} \quad (3.34)$$

The dispersed phase pressure is the product of a function of volume fraction  $\zeta$  multiplied by the internal pressure. Below and above the volume fraction limits,  $\zeta$  is constant, equaling either zero or one. In the transition regime,  $\zeta$  is assigned a power law dependence on the normalized volume fraction, which forces the boundary conditions to be met.

The proposed form of the dispersed phase equation of state (3.34) produces the expected behavior in sound speed. When  $\alpha_D \leq \alpha_{min}$ ,  $P_D = 0$  regardless of the material density and energy, so that the sound speed  $c_D$  is also zero. This corresponds with the assumption of non-interacting particles that do not communicate directly with one another. When  $\alpha_D \geq \alpha_{max}$ ,  $P_D = P_{int,D}$  and the functional dependence on volume fraction vanishes; hence  $c_D = c_{int,D}$ . The proper prediction of the sound speed is important as it is directly applied in the Riemann solver.

This approach to constructing an equation of state for a dispersed phase material is attractive as it requires only knowledge of an equation of state for the pure material, which also defines the internal pressure of the particles, and the definition of the parameters  $\alpha_{min}$ ,  $\alpha_{max}$ , and  $z$ . While an equation of state for the pure material is likely to be available in the literature, the other parameters must be estimated or fit to experiment. Physically, it is unlikely that a canonical set of values will exist, as the behavior of a dispersed phase material is likely to

be dependent material specific factors such as particle shape. However, in the absence of an accurate theoretical model for the dispersed phase pressure in shock driven environments, the heuristic approach provides a simple and robust method for capturing the behavior of a collection of particles in flow regimes ranging from dense to dilute.

## Chapter 4

### Comparison with Experiment

In this chapter, two multiphase explosion scenarios are investigated numerically. The scenarios are chosen to align with existing experimental data in order to validate the numerical modeling methodology and results. Both scenarios involve the detonation of a multiphase explosive charge consisting of an ideal explosive mixed with inert solid particles. Initial particle loadings vary widely, ranging from a fully packed bed with 62% particles by volume in one case to only 10% particles by volume in the other. Results include the transient motion of the leading particle and shock fronts, as well as range-dependent pressure data. Excellent agreement is found between the model and experiment, providing confidence in the numerical modeling methodology proposed in Ch. 3.

Before comparing the simulations with experiment, a note on the governing equations is in order. With reference to the nozzling terms, which were discussed in Sec. 2.3.2, all results presented in this work were produced by setting  $P_{s,k} = P_k$  and  $P_i = 0$ . Simulations were also attempted using the traditional form of the nozzling terms ( $P_{s,k} = P_i$ ), with the interfacial pressure set to that of the continuous phase ( $P_i = P_C$ ), as in the work of Baer and Nunziato [1]. However, the additional acceleration produced by the last term in Eq. 2.33 produced erroneously high particle accelerations that caused numerical instability. The regions in which such

problems occurred were typically near the particle front, where the particle flow was dilute and the dispersed phase pressure – and pressure gradient – were zero. In these cases, it is difficult to justify the application of the force produced by the last term in Eq. 2.33. Because of the erroneous results, and lack of physical justification, this form of the governing equations was not used.

## 4.1 Multiphase Explosion Simulation #1

The first multiphase explosion investigated is based on the experimental work of Zhang et al. [32], which investigated the explosive dispersal of solid particles. In the experiments, a multiphase explosive charge was detonated in air, and data on the time evolution of the leading shock and particle fronts was collected, in addition to pressure data. The explosive charge was spherical and consisted of a fully-packed bed of 463  $\mu\text{m}$  spherical steel particles saturated with sensitized nitromethane. The charge was mounted above the ground and centrally detonated, resulting in an approximately spherical explosion in the time-frame of interest. Further details on the experimental setup can be found in the original publication [32].

Numerical simulations of this experiment were performed in 1-D spherical coordinates. Prior to the passage of the detonation front, the liquid nitromethane was represented with a Mie-Gruneisen equation of state formulation [11], while the detonation products and surrounding air are treated with the traditional Jones–Wilkins–Lee (JWL) formulation [14, 11]. The steel particles are treated with the heuristic equation of state approach proposed in Sec. 3.3, with a Mie-Gruneisen formulation representing the internal pressure. The detonation process was modeled with the history variable reactive burn (HVRB) method [11]. Equations of state and reactive burn parameters for the materials used in this study can be found in Ref. [11].

The fully-packed nature of the initial particle configuration makes accounting for the dispersed phase pressure key to accurately simulating this multiphase explosion scenario. Initially, the particles are in direct contact with one another leading to strong interaction. However, as the explosion products expand, the spacing between particles quickly increases and the volume fraction drops, such that direct particle interactions become negligible and the dispersed phase pressure becomes zero. This functional dependence of pressure on volume fraction is modeled with the heuristic equation of state in Eq. (3.34). To close this equation, the parameters  $\alpha_{min}$ ,  $\alpha_{max}$ , and  $z$  must be set. For simplicity,  $z$  is set to one in the current simulation; this choice results in a linear decay of the dispersed phase pressure with respect to volume fraction. Further, it is postulated that when fully packed, the pressure felt at the interface between two particles is approximately equal to the internal pressure of the particles; therefore  $\alpha_{max}$  was set to 0.62, which is the fully packed volume fraction measured in the experiment. Given these parameters,  $\alpha_{min}$  was determined through a series of trial simulations and is set a 0.2. Sensitivities of the simulation results to these parameters are discussed in the following chapter.

Results from the numerical simulation are presented at selected times in Figs. 4.1-4.4. The continuous phase (nitromethane and air) velocity is shown, along with the dispersed phase (particle) velocity and volume fraction. The particles are initially accelerated by a combination of the dispersed phase pressure gradient and the drag force resulting from velocity non-equilibrium with the surrounding fluid. As the particles expand outwards, the volume fraction quickly drops, removing the influence of the dispersed phase pressure. A consequence of this is that the particle velocity is no longer reduced by the effects of volumetric expansion. The continuous phase velocity, however, is affected by the volumetric expansion and drops as the shock front propagates radially outward. These factors allow the

particle front, which initially trails the shock front in the continuous phase, to catch and surpass the leading shock at approximately 0.5 ms. Once past the shock front, the particle front continues to separate from the shock within the time-frame shown. The ability of the particles to run-away from the shock is a function of the particle momentum, which in this case is relatively large because of the particle size, density, and velocity.

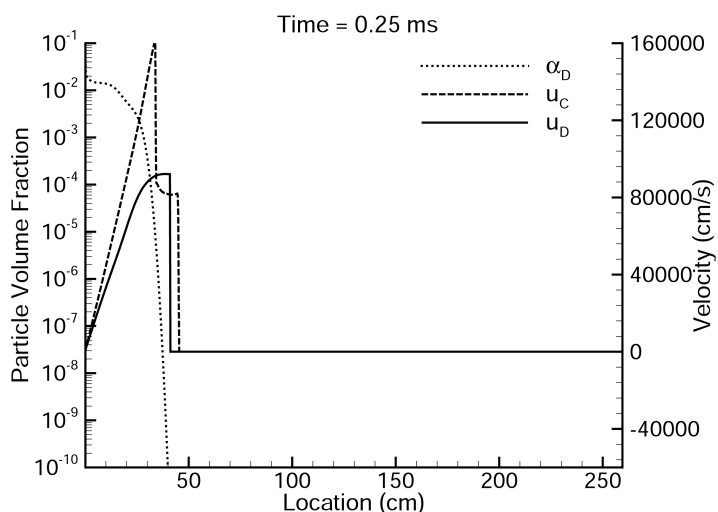


Figure 4.1: Velocity and volume fraction profiles at 0.25 ms for explosion of nitromethane charge with 463  $\mu m$  steel particles; 62% initial particle loading by volume.

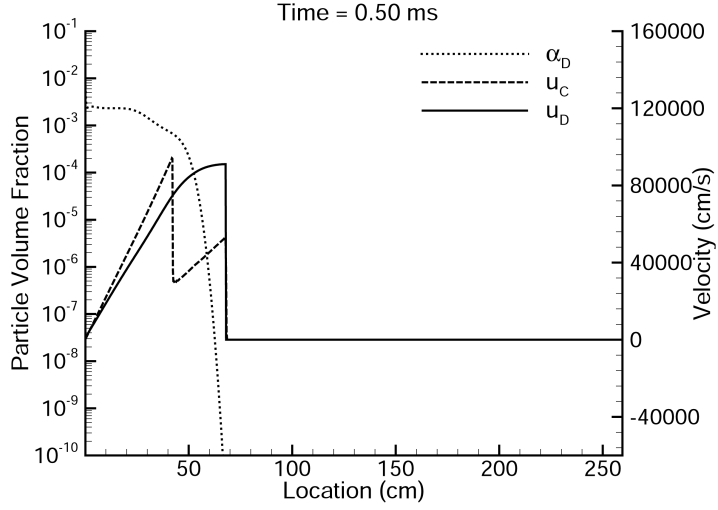


Figure 4.2: Velocity and volume fraction profiles at 0.50 *ms* for explosion of nitromethane charge with 463  $\mu\text{m}$  steel particles; 62% initial particle loading by volume.

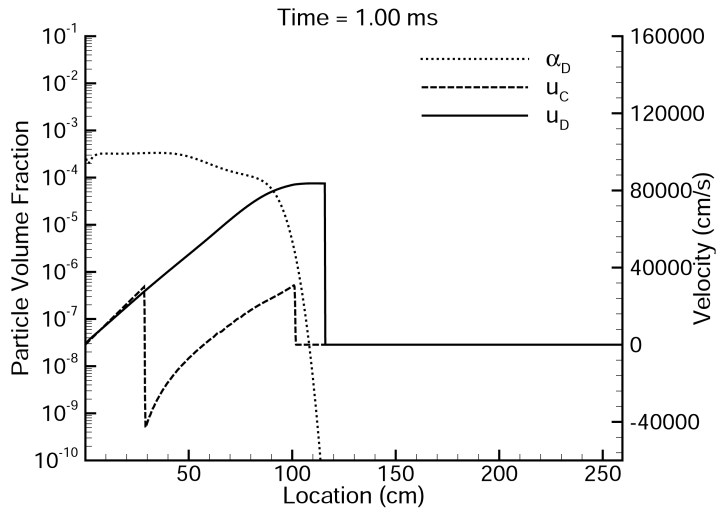


Figure 4.3: Velocity and volume fraction profiles at 1.00 *ms* for explosion of nitromethane charge with 463  $\mu\text{m}$  steel particles; 62% initial particle loading by volume.

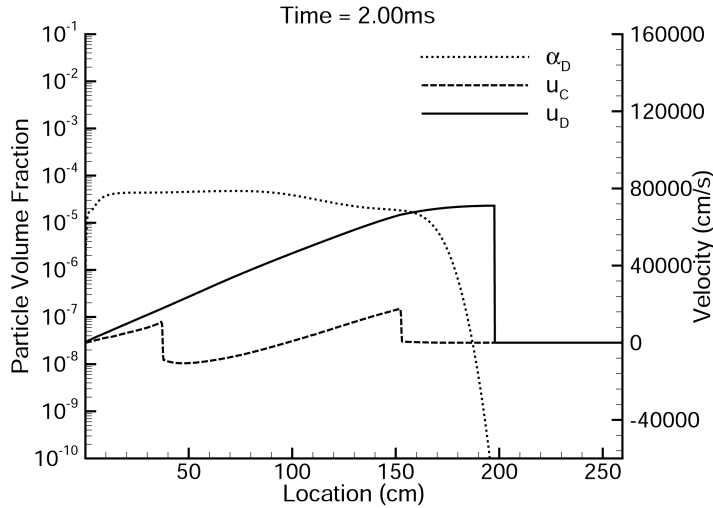


Figure 4.4: Velocity and volume fraction profiles at 2.00 *ms* for explosion of nitromethane charge with 463  $\mu\text{m}$  steel particles; 62% initial particle loading by volume.

Fig. 4.5 compares the numerical and experimental trajectories of the leading shock and particle fronts with respect to time. The experimental values have been digitized from the original work of Zhang et al. [32]. The numerical results summarize the phenomena illustrated in Figs. 4.1-4.4 and discussed above. The shock front leads the particle front until approximately 0.5 *ms*, at which point the particle front overtakes the shock. The particle front then continues to separate from the shock over the time-frame shown. The experimental data collected by Zhang et al. [32] agrees well with the numerical results. The data shows that the particle front escapes the shock between 0.4 and 0.6 *ms*, which closely bounds the numerically predicted escape time of 0.5 *ms*. The experimental trajectories for both the shock and particle fronts also agree well with the numerical results before and after the time of escape.

Fig. 4.6 compares the numerical and experimental peak pressures with respect to distance from the charge. Results are shown both for the nitromethane

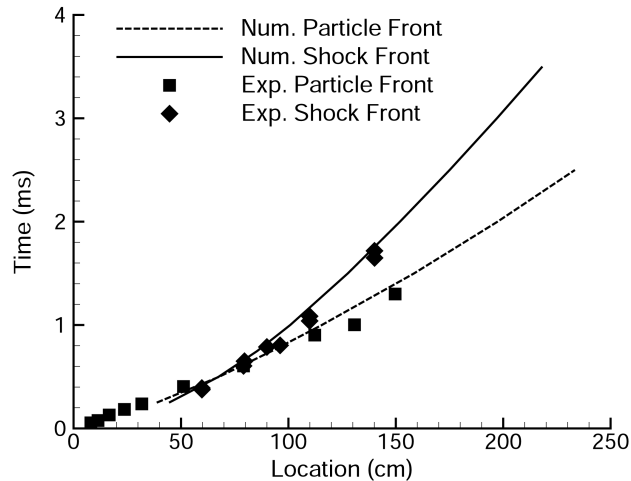


Figure 4.5: Comparison of experimental and numerical shock and particle front locations from the detonation of a nitromethane charge with  $463 \mu\text{m}$  steel particles; 62% initial particle loading by volume.

charge containing steel particles described above, and for a pure nitromethane charge of the same diameter. Peak pressures for the pure nitromethane charge are also digitized from the original work of Zhang et al. [32]. In both cases, the numerical results closely match the experimental data. The model correctly predicts the reduction in peak pressure that occurs with the addition of particles. This reduction in pressure is a function of both the reduced mass of energetic material in the charge, and the transfer of momentum and energy from the high explosive to the particles.

The close agreement between the experimental data of Zhang et al. [32] and the numerical simulation results serve to validate the modeling techniques proposed in Ch. 3. The multiphase Riemann solver and heuristic equation of state, combined with the phase interaction models applied, accurately predict the explosion dynamics of the charge investigated. The dynamics of this event are complex; as

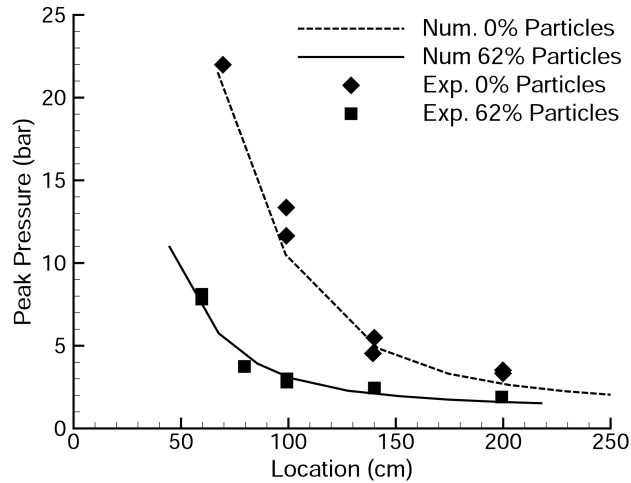


Figure 4.6: Comparison of experimental and numerical peak pressures from pure nitromethane and nitromethane/steel particle explosions.

the explosion products expand the particle volume fraction transitions from dense to dilute, and strong velocity non-equilibrium exists among the phases throughout the time-frame of interest. The numerical modeling techniques reproduce these effects well, demonstrating the ability of the model to predict challenging multiphase explosion phenomena.

## 4.2 Multiphase Explosion Simulation #2

The second multiphase explosion simulation performed is based on experiments performed by Carney and Lightstone [3]. Unlike the charges of Zhang et al. [32] which consisted of fully-packed particle beds, these explosives have a more moderate initial particle loading. The multiphase charges investigated consist of PETN mixed with spherical soda-lime glass particles. PETN is a relatively sensitive solid explosive that detonates fully at the charge sizes of interest. Its detonation products are clear allowing for the use of optical diagnostic techniques.

The glass particles are  $3 \mu\text{m}$  in diameter and are loaded at an initial volume fraction of 0.10. The explosive charges are 1 inch right cylinders with a length to diameter ratio of one. They were suspended in air and detonated in the center of the top face of the cylinder. Fast-framing camera images taken in a shadowgraph configuration provide the particle and shock front locations at multiple times.

Numerical modeling of this experiment was performed in 2-D cylindrical coordinates. The PETN was modeled using a Mie-Gruneisen [11] equation of state before the passage of the detonation front, and a JWL [14, 11] equation of state afterwards. The air was likewise modeled with a JWL equation of state. The dispersed particle phase was again modeled using the heuristic equation of state proposed in Sec. 3.3, with a Mie-Gruneisen formulation representing the internal pressure. However, because the initial particle volume fraction of 0.10 is below the value of  $\alpha_{min}$  applied in the first simulation, dispersed phase pressure effects were not effective in this simulation.

Results from the numerical simulation are compared with images from the experiment in Figs. 4.7 and 4.8. These results are taken at 10 and 20  $\mu\text{s}$  after detonation, respectively. The numerical images include 2-D contours of particle volume fraction, as well as lines denoting the locations of the shock and detonation product fronts. The numerical results show that nearly the entire volume behind the shock front contains particles, but that virtually no particles exist outside the shocked region. While the particles are sufficiently accelerated to escape the detonation products, they do not efficiently escape the leading shock. This is in contrast to the the results shown in Sec. 4.1, where the particles surpass and separate from the shock. The particles in the current simulation are two orders of magnitude smaller than those in the previous simulation, in addition to being less dense. Because of this, the particles have significantly less momentum than the larger particles investigated previously, even if accelerated to equivalent velocities.

The reduced particle mass and momentum are responsible for the inability of the particles to escape the leading shock. When particles attempt to pass the leading shock, they immediately experience an increased drag force as they enter the ambient atmosphere. The increased drag quickly reduces the momentum of the particles, which are then recaptured by the shock. This effect was discussed previously by McGrath, et al. [16].

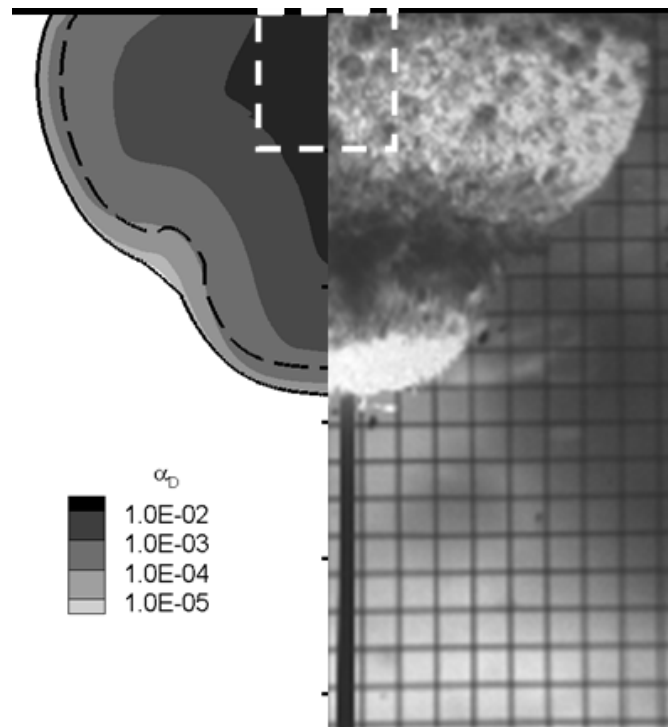


Figure 4.7: Comparison of numerical contours and experimental image  $10 \mu s$  after explosion of PETN charge with  $10 \mu m$  glass particles. Numerical results include contours of particle volume fraction ( $\alpha_D$ ), solid line indicating shock front, and dashed line indicating detonation product front. Dashed white line indicates initial charge geometry.

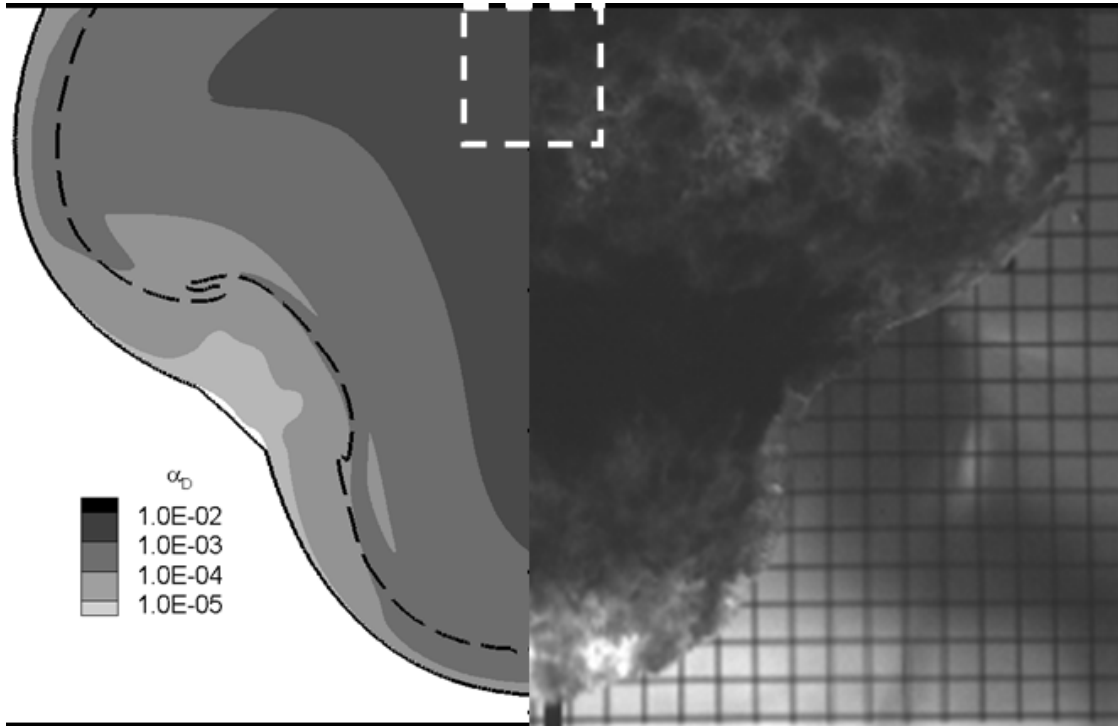


Figure 4.8: Comparison of numerical contours and experimental image  $20 \mu s$  after explosion of PETN charge with  $10 \mu m$  glass particles. Numerical results include contours of particle volume fraction ( $\alpha_D$ ), solid line indicating shock front, and dashed line indicating detonation product front. Dashed white line indicates initial charge geometry.

The numerical results are strongly supported by the images from the experiment. While the detonation products of pure PETN are optically clear, this clarity is removed in locations where particles are present. As predicted by the model, nearly the entire volume behind the leading shock front is observed to contain particles in the experiment. The particle front is aligned with the shock front except in isolated areas of the  $20 \mu s$  image. In this image, the shock leads the particles by a small distance near the elbow of the blast where the radial and axial plumes meet. These areas are similar to those predicted to have the smallest volume fraction of

particles as shown by the contours.

To better quantify the numerical and experimental results, the location of the leading particle front was tracked with respect to time along a line broadside of the charge. The results of this comparison are shown in Fig. 4.9. Excellent agreement between the experimentally measured and numerically predicted particle front trajectories is found. The numerical results lie well within the error of the experiment. Hence the model produces not only good qualitative agreement with experiment, but also good quantitative agreement. These results further validate the numerical modeling techniques proposed in this work.

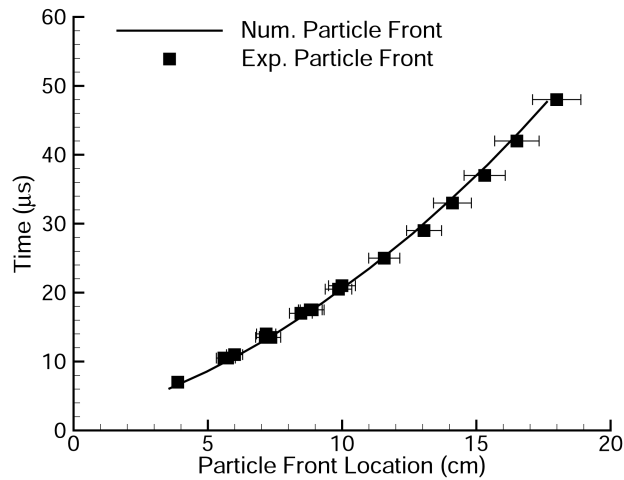


Figure 4.9: Comparison of experimental and numerical particle front trajectories broadside of PETN/glass particle explosion.

## Chapter 5

# Sensitivity to Correlations for Drag, Heat Transfer, and Dispersed Phase Pressure

This chapter examines the sensitivity of the numerical solutions to correlations for drag, heat transfer, and particle phase pressure. Investigating these sensitivities is important to understanding the relative effect individual terms have on the calculated solution and, in the case that multiple correlations are available, determining which provides the best comparison with experiment. The comparisons also quantify the importance of properly accounting for the physical nature and mathematical characteristics of dispersed materials. This result is important in the context of the disagreement over the dispersed phase pressure that exists in the literature, which was discussed in Sec. 2.3.1. This chapter is divided into three sections that individually investigate the effect of drag correlations, heat transfer, and dispersed phase pressure on the calculated results. Simulations are based on the experiment performed by Zhang et al. [32], which was discussed in Ch. 4. This scenario was chosen because it: 1) contains the largest amount of experimental data to compare to, 2) has a high enough initial particle loading that particle pressure effects are important, and 3) can be simulated in 1-D, easing the computational time required to perform the study.

## 5.1 Sensitivity to Drag Correlations

The basic methodology used to model the drag force was discussed in Sec. 3.2. In this section, the standard drag correlation for an isolated sphere was replaced by the method of Wen and Yu [31] to account for volume fraction effects. The net effect of this correction is that drag force increases with increasing particle volume fraction. However, at sufficiently high volume fractions (typically above  $\alpha_D = 0.2$ ) Crowe et al. [4] suggest the use of an alternate expression. In Sec. 3.2, the correlation of Shepherd and Begeal [26], which was used in the work of Bear and Nunziato [1], was introduced for use in these conditions. However, the correlation proposed by Ergun [7] in his study of fluid flow through packed columns is another alternative. Ergun’s expression for drag force is is:

$$f = \frac{\mu_C \alpha_D}{D^2 \alpha_C^2} (1.75 \alpha_C Re_R + 150 \alpha_D) (u_C - u_D) \quad (5.1)$$

Four different methods of calculating the drag force are investigated in the current study. The methods vary in the way that the effects of volume fraction are handled. As a baseline, the drag force on a single particle with no correction for volume fraction is considered. Next, the correction of Wen and Yu [31] is considered alone, without the use of an alternate expression when  $\alpha_D \geq 0.2$ . Finally, the correction of Wen and Yu is again considered, but with the use of the alternate expressions of Ergun and Shepherd & Begeal when  $\alpha_D \geq 0.2$ . The four methods of calculating drag force along with the naming convention used for each are listed below:

1. Single Particle: no volume fraction correction
2. Wen: volume fraction correction of Wen & Yu only
3. Ergun: correction of Wen & Yu for  $\alpha_D < 0.2$ , Ergun correlation for  $\alpha_D \geq 0.2$

4. Shepherd: correction of Wen & Yu for  $\alpha_D < 0.2$ , Shepherd & Begeal correlation for  $\alpha_D \geq 0.2$

Before investigating the effect of these drag correlations on the numerical results, it is instructive to examine the forces predicted by the correlations being considered. These are plotted over a range of Reynolds numbers and particle volume fractions in Fig. 5.1. Here, all drag forces have been non-dimensionalized by the drag force on a single particle ( $f_{S.P.}$ ). Only conditions under which the Ergun and Shepherd expressions are typically used ( $\alpha_D \geq 0.2$ ) are considered.

From Fig. 5.1, it is observed that the force predicted by the Wen correlation increases from 2.3X-30X that predicted for a single particle over the range of  $\alpha_D = 0.2 - 0.6$ . Because the Wen correlation corrects the single particle drag force as a function of volume fraction only, the result is invariant with Reynolds number. Comparing the Ergun and Shepherd correlations to that of Wen, it is observed that the force produced by the Ergun correlation is generally greater than that of Wen in the case of  $\alpha_D = 0.2$ , approximately equal to it for  $\alpha_D = 0.4$ , and less than it for  $\alpha_D = 0.6$ . The Shepherd correlation produces substantially larger drag forces than either of the other methods. Over the range of conditions shown in Fig. 5.1, it varies from 2X-25X the force produced by the Wen correlation, and 4X-10X that produced by the Ergun correlation. Based on these results, it is clear that the options presented produce significant differences in the magnitude of the drag force predicted.

To investigate the effect of the different drag correlations on the calculated results, numerical simulations replicating the experimental work of Zhang et al. [32] have been performed. In the simulations, the effects of dispersed phase pressure were purposefully neglected by setting  $\zeta = 0$ ; this isolates drag as the lone source of particle motion, allowing for a more direct comparison of the results. Numerical

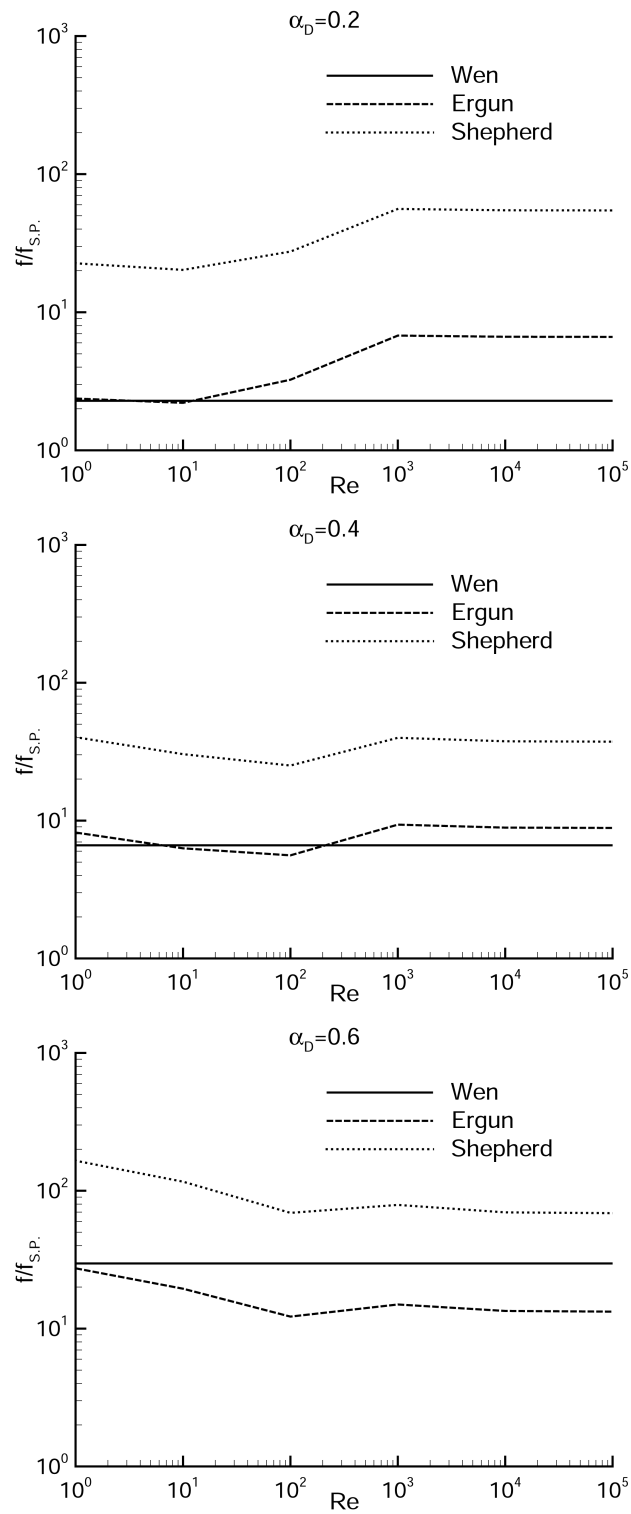


Figure 5.1: Comparison of drag force correlations.

results are compared with the experimental data in Fig. 5.2. The results include plots of shock propagation, peak pressure, and particle front trajectory. Among the various drag correlations accounting for volume fraction effects, little difference is observed in the predicted shock front location or peak pressure. The shock trajectories are nearly identical, and the peak pressures are similar, with the pressure observed using the Shepherd correlation being slightly lower than the others. When the drag correlation for a single particle is used however, larger differences occur. In this case, the shock front leads that calculated by any of the other methods, and the peak pressures are higher. In the near-field, the pressure observed is visibly higher than the data reported from the experiment [32]. When considering the effects on particle motion, the single particle drag force produces the smallest particle front velocity, while the Shepherd method produces the largest. None of the calculated particle front trajectories compare well with the experimental data in this case because the dispersed phase pressure was neglected.

The trends observed in the calculated results are consistent with those expected given the force comparison shown in Fig. 5.1. The single particle drag correlation results in the smallest interaction force between the continuous and dispersed phase, allowing a faster and stronger shock to propagate into the surrounding environment, and reducing the velocity of the particles. On the other hand, the Shepherd method produces the largest drag force; this accelerates the particles more rapidly and restricts the continuous phase flow, resulting in reduced shock velocity and peak pressure. It is interesting to note, however, that the variation among the results produced by the Shepherd, Ergun, and Wen methods is minimal. While this may initially be unsuspected given the variations in drag force shown in Fig. 5.1, one must recall that despite the naming convention used, the Ergun and Shepherd correlations become active only in conditions where  $\alpha_D \geq 0.2$ , which for the current problem is a relatively small percent of the simulated time.

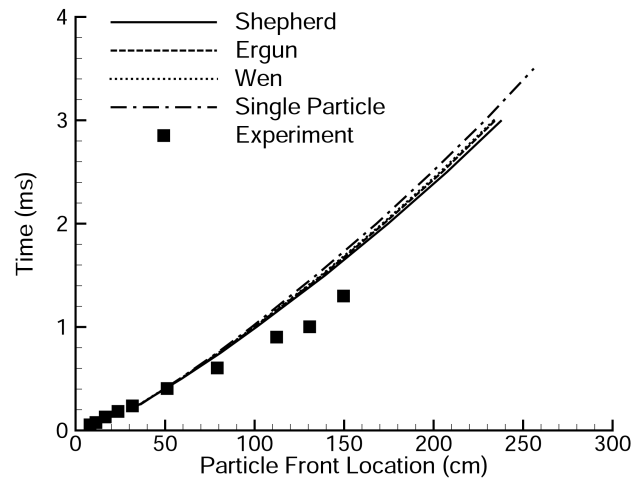
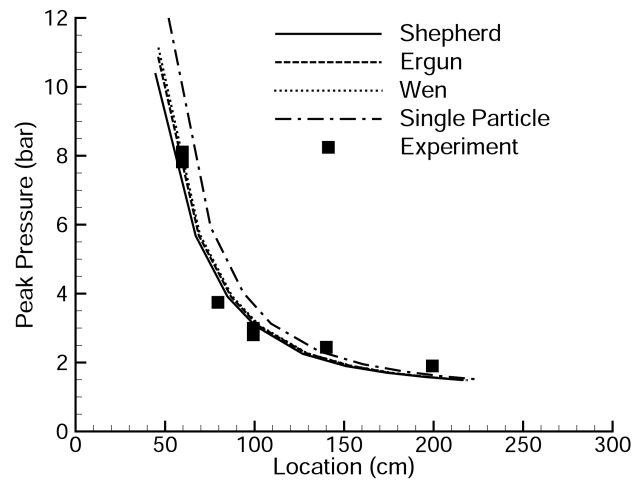
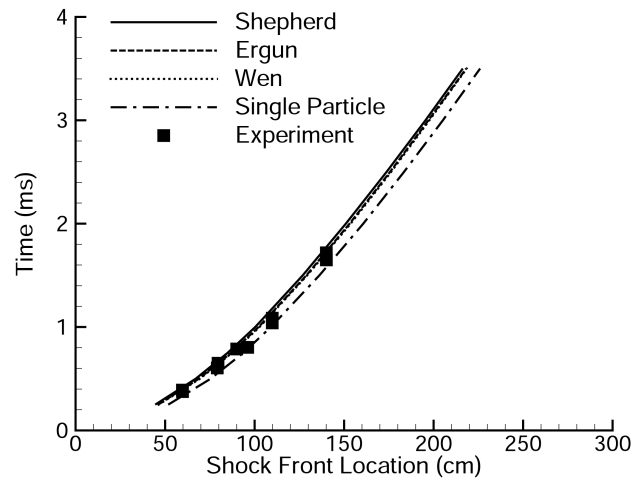


Figure 5.2: Effect of drag correlations on shock propagation, peak pressure, and particle front location.

Overall, the results indicate that accounting for volume fraction effects in the drag correlation improves the accuracy of the predicted shock velocity and pressure. However, they do not support a definitive conclusion on the particular drag correlation to use in cases where  $\alpha_D \geq 0.2$ . A more definitive conclusion may require analyzing scenarios in which the volume fraction of the particle flow remains above 0.2 for longer periods of time.

## 5.2 Sensitivity to Heat Transfer

In this section, the sensitivity of the computed results to heat transfer are investigated. In all simulations conducted to this point, heat transfer is calculated using the correlation presented in Sec. 3.2, which models the convective heat flux as a function of the temperature difference among phases, as well as the Nusselt number. To determine the sensitivity of the calculated solution to this expression, numerical simulations have been performed in which the rate of heat transfer is modified by the inclusion of a multiplicative factor in Eq. (3.29). Three cases have been investigated, using factors of 0, 1, and 2. Thus, in addition to the baseline rate defined by Eq. (3.29), the rate of heat transfer has been either completely neglected or doubled.

The numerical simulation setup used for this study is identical to that presented in Sec. 4.1, with the only exception being the multiplicative factor included in the heat transfer correlation. The drag force was calculated using the correction of Wen and Yu [31] when  $\alpha_D < 0.2$ , and the correlation of Shepherd and Begeal [26] for  $\alpha_D \geq 0.2$ . Particle phase pressure effects were accounted for using the parameters described in Sec. 4.1.

The maximum particle temperatures observed at selected times are shown in Tab. 5.1 for each of the three heat transfer rates considered. Here, it is observed

that the multiplicative factors applied to the base correlation have a meaningful effect in terms of temperature variation during the time-frame considered. When heat transfer is neglected, a drop of 86-93  $K$  in maximum particle temperature is observed when compared to the baseline simulation. Doubling the heat transfer rate results in approximately a 60  $K$  increase in maximum particle temperature over the baseline simulation.

Factor	Time after Detonation		
	<i>0.5 ms</i>	<i>1.0 ms</i>	<i>2.0 ms</i>
0	314 $K$	314 $K$	314 $K$
1	400 $K$	407 $K$	405 $K$
2	461 $K$	469 $K$	465 $K$

Table 5.1: Maximum particle temperatures calculated using various heat transfer rates

Results from the simulations are compared with the experimental data of Zhang et al. [32] in Fig. 5.3. From this, it is observed that the variation in heat transfer rate does have a measurable, although small, effect on the numerical results. As the rate of heat transfer is increased, both the shock and particle front velocities are reduced, as is the peak pressure. When compared to the experimental data, the variations are sufficiently modest that any of the results would perhaps be considered acceptable, although those computed with either the factor of 0 or 1 compare best. This trend suggests that the heat transfer rates predicted by Eq. (3.29) are within a reasonable range for the current simulation. While the data would imply that the rate of heat transfer should not be increased, neither does it strongly suggest that the rate should be decreased.

Overall, it is instructive to note that the rate of heat transfer used in the numerical simulation does have a quantifiable, although minor, effect on readily observable parameters such as shock propagation, pressure, and particle motion.

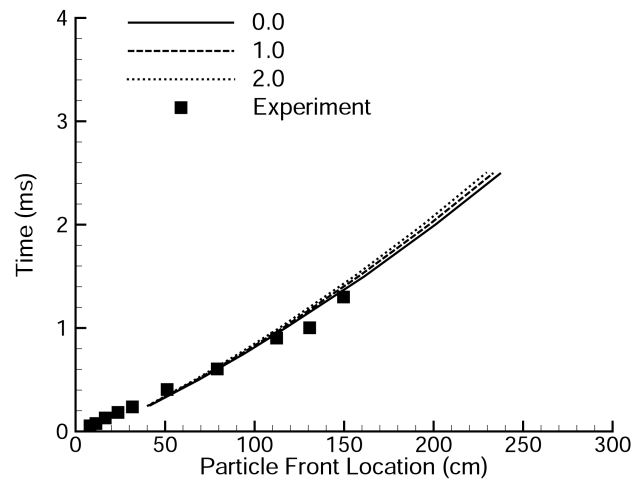
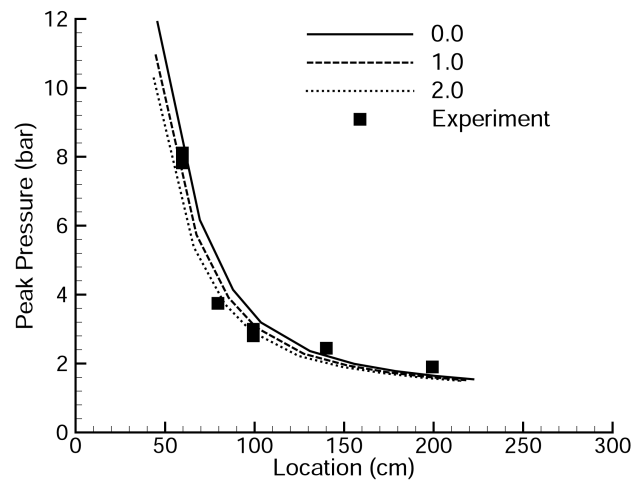
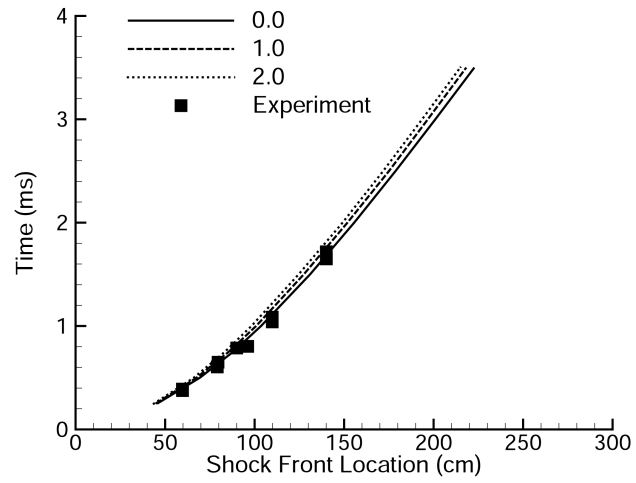


Figure 5.3: Effect of heat transfer on shock propagation, peak pressure, and particle front location.

Intuitively, the physical trend observed here may be expected when the physics of the situation are considered. Heat transfer among the various phases in a multi-phase flow is a dissipative process that reduces the amount of energy available to do work in the system. This results in the reduction in pressure, shock velocity, and particle velocity observed. While this physical trend may be expected, the magnitude of the effect would be difficult to discern without the benefit of the current numerical analysis.

### 5.3 Sensitivity to Dispersed Phase Pressure

Having investigated the sensitivity of the computed results to drag and heat transfer, attention is turned to the effects of dispersed phase pressure. Recall from Sec. 2.3.1 that methods for representing the dispersed phase pressure  $P_D$  vary in the literature. In this work, as in others [4, 8, 32], it is argued that the pressure exerted by a dispersed material comes about through particle interactions resulting from contact or collisions. This argument leads to the functional dependence of  $P_D$  on volume fraction, which is a measure of particle spacing. Based on this argument, a model for calculating  $P_D = P_D(\alpha_D, \rho_D, e_D)$  was proposed in Eq. (3.34) of Sec. 3.2. In other influential models relating to multiphase explosions [1, 10, 25, 2, 13], however,  $P_D$  is not considered to be a function of  $\alpha_D$  at all. Rather it is calculated as  $P_D = P_D(\rho_D, e_D)$ , making the pressure of the phase equal to that inside the individual particles. Based on the arguments in the current work, this can only be justified in regimes of very high particle volume fractions. Yet another technique is to ignore the dispersed phase pressure completely. This assumption is typically made in works focusing exclusively on dilute particle flows, such as those of Papalexandris [17, 18]. Under the proposed theoretical picture of dispersed phase pressure, this assumption is justified as long as the flow exists in the dilute

regime.

This section has two objectives. The first is to investigate the effect different representations of dispersed phase pressure have on the numerical solutions. The second is to investigate the sensitivity of the predicted results to the parameters,  $\alpha_{max}$ ,  $\alpha_{min}$ , and  $z$ , that influence the behavior of the proposed model for  $P_D$  (3.34). The former objective directly addresses the physical nature of the pressure of a dispersed material, while the latter reveals information relevant to the proper modeling of these materials.

### 5.3.1 Sensitivity to Dispersed Phase Pressure Representation

First, the influence of different representations of particle phase pressure are addressed. Three distinct representations of  $P_D$  are considered; these are: 1)  $P_D = 0$ , 2)  $P_D = P_{int,D}$ , and 3)  $P_D = \zeta(\alpha_D) P_{int,D}$ . In the first representation, the dispersed phase pressure is neglected completely, which implies that particle-particle interactions are unimportant. The second representation aligns with many influential models [1, 10, 25, 2, 13] that assume the dispersed phase pressure is equivalent to that within an individual particle. The third aligns with the theory of dispersed material pressure presented in the current work. Here,  $P_D$  is modeled as a function of volume fraction, as proposed in Eq. (3.34). In this study, the calculations performed are identical with the exception of the representation of  $P_D$ . The correlations for drag and heat transfer are those presented in Sec. 3.2. In the case where  $P_D = \zeta(\alpha_D) P_{int,D}$ ,  $\zeta$  is defined using the parameters:  $\alpha_{max} = 0.62$ ,  $\alpha_{min} = 0.20$ , and  $z = 1$ , which are identical to those applied in Sec. 4.1.

Numerical results are compared with those from the experiment [32] in Fig. 5.4. In the case of the shock trajectories and peak pressures, it is observed that the different representations of  $P_D$  produce results that are nearly identical to one another, and closely match the experimental data. When the plot of particle

front location is considered, however, significant differences among the modeling approaches are observed. Here, the case in which  $P_D = P_{int,D}$  results the slowest particle front velocity, while the case in which  $P_D = \zeta(\alpha_D) P_{int,D}$  provides the fastest. When  $P_D = 0$ , the front velocity falls between the other cases, but tends toward the slower side, being only slightly faster than the result for  $P_D = P_{int,D}$ . From the results, it is also clear that the case in which  $P_D = \zeta(\alpha_D) P_{int,D}$  provides the best match with the experimental data.

To understand the physics driving these results, the dynamics of each scenario must be considered. The simplest case is that in which  $P_D = 0$ . Here, because the pressure of the dispersed phase is universally zero, no pressure gradient force exists to accelerate the particle flow. The particle motion is purely the result of interphase drag caused by velocity non-equilibrium among the phases.

Next consider the case in which  $P_D = P_{int,D}$ . The internal pressure  $P_{int,D}$  is defined through the equilibration process with the continuous phase (explosive and air). Because the continuous phase pressure  $P_C$  always exists,  $P_{int,D}$  and therefore  $P_D$  are universally non-zero. In fact, pressure equilibrium ensures that  $P_C = P_D$ , meaning that equal pressure gradients exist in both phases. After the charge detonates, a large pressure gradient accelerates both phases outward. Expansion effects, however, quickly reduce the pressure and set up an inverse pressure gradient, slowing the flow. The important point to recognize is that by assuming  $P_D = P_{int,D}$ , the inverse pressure gradient affects both phases, which serves to reduce the particle velocity. It is for this reason that the particle front velocity when  $P_D = P_{int,D}$  is observed to be slower than when  $P_D = 0$ .

Finally, consider the result produced when  $P_D = \zeta(\alpha_D) P_{int,D}$ . In this case,  $P_D$  only exists when  $\alpha_D > \alpha_{min}$ , where  $\alpha_{min} = 0.2$  in the current simulation. The initial charge configuration has 62% particles by volume, making  $P_D$  non-zero during the detonation. Thus both the pressure gradient force and interphase drag

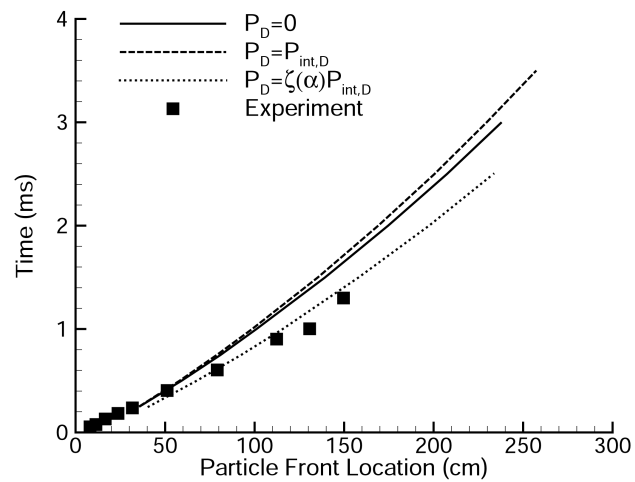
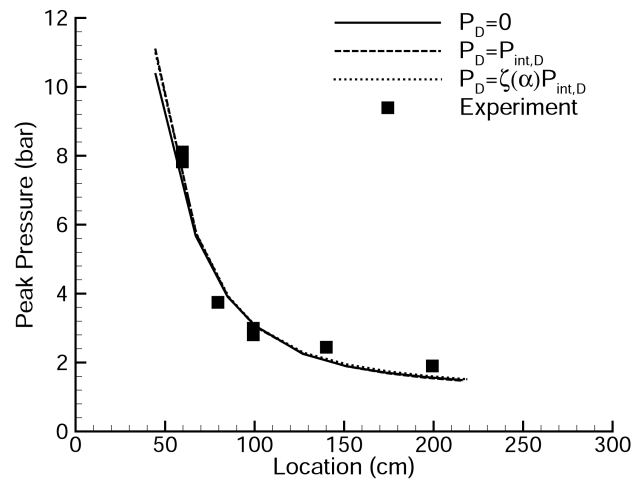
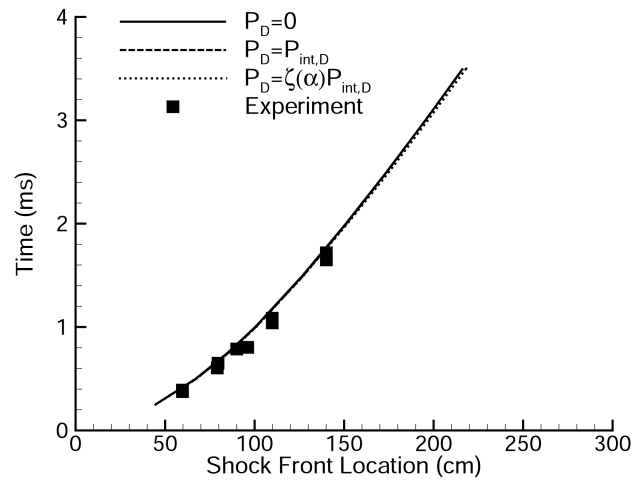


Figure 5.4: Effect of dispersed phase pressure on shock propagation, peak pressure, and particle front location.

force are available to initiate particle motion. As the particles expand outward, however,  $\alpha_D$  quickly drops below  $\alpha_{min}$ , and  $P_D$  becomes zero. At this point, a pressure gradient no longer exists in the dispersed phase and only the drag force affects the particles. In Fig. 5.5, it is observed that by 0.25 ms, which corresponds to the first numerical time plotted in Fig. 5.4, the particle volume fraction has already dropped below the threshold for non-zero  $P_D$ . By applying  $P_D = \zeta(\alpha_D) P_{int,D}$ , the initial particle acceleration is increased over the case in which  $P_D = 0$  because of the pressure gradient force. However, the functional dependence on  $\alpha_D$  quickly removes the pressure gradient force, shielding the particles from the reduction in velocity that subsequently occurs in the case of  $P_D = P_{int,D}$ . It is for this reason that the case of  $P_D = \zeta(\alpha_D) P_{int,D}$  produces the fastest particle front velocity in Fig. 5.4.

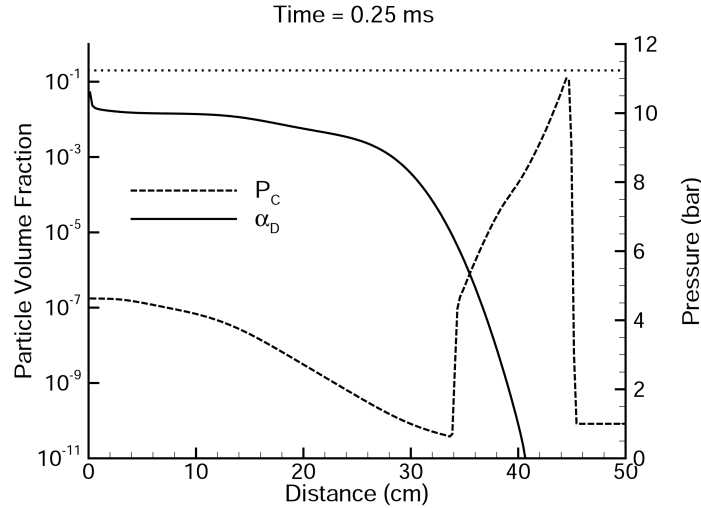


Figure 5.5: Profiles of pressure and particle volume fraction for the case of  $P_D = \zeta(\alpha_D) P_{int,D}$ . Dotted line indicates threshold volume fraction.

The results of this comparison are important in the context of the disagreement on the representation of dispersed phase pressure that exists in the literature. The current analysis clearly demonstrates that different representations of

$P_D$  produce substantially different results. By comparing the various representations of  $P_D$  with the experimental findings reported by Zhang et al. [32], it becomes apparent that  $P_D$  is a function of  $\alpha_D$ , as argued in Sec. 2.3.1, and that accounting for this dependence is critical to obtaining accurate numerical predictions. Furthermore, the close agreement with the experimental results suggests that the proposed model for dispersed phase pressure (3.34) accurately represents the behavior of such materials under the conditions encountered in the current simulation. Determining the range of conditions in which this agreement is seen requires a broader range of experiments not currently provided in the literature. Further validation is therefore the subject of ongoing work.

### 5.3.2 Sensitivity to $\alpha_{max}, \alpha_{min}$ , and $z$

Having shown the importance of modeling the functional dependence of dispersed phase pressure on volume fraction, the sensitivity of the proposed model for  $P_D$  (3.34) to the parameters  $\alpha_{max}$ ,  $\alpha_{min}$ , and  $z$  is investigated. These parameters are critical to obtaining accurate simulation results, as they define the transition regime between dense particle flows in which pressure effects are important, and dilute regimes in which they are not. From Eq. (3.34), the function  $\zeta$  determines the dependence of  $P_D$  on  $\alpha_D$ . This dependence is schematically represented in Fig. 5.6. The transition regime exists between the parameters  $\alpha_{min}$  and  $\alpha_{max}$ , with the shape of the function in this regime being defined by the parameter  $z$ .

In the following analyses, the set of parameters used previously is taken as a baseline; they were:  $\alpha_{max} = 0.62$ ,  $\alpha_{min} = 0.20$ , and  $z = 1$ . Each of these parameters is varied around its baseline value, while the others are held fixed. Results are then plotted against the experimental data, revealing not only the trend encountered when the parameter is varied, but also the effect of the variation on the solution accuracy.

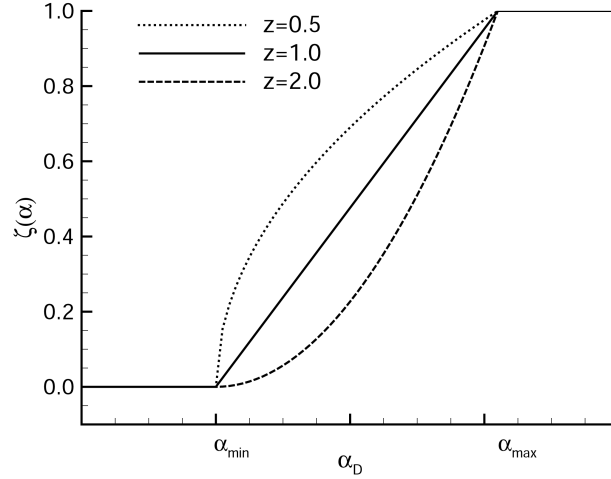


Figure 5.6: Functional dependence of  $\zeta$  with respect to  $\alpha_{max}$ ,  $\alpha_{min}$ , and  $z$ .

### Sensitivity to $\alpha_{max}$

First the parameter  $\alpha_{max}$  is considered. This parameter defines the upper bound of the transition regime; for  $\alpha_D \geq \alpha_{max}$ ,  $\zeta = 1$  and  $P_D = P_{int,D}$ . The baseline value of  $\alpha_{max}$  was previously set to align with the fully-packed state of the particle bed from the experiment [32], which was 0.62. This was based on the postulate that in its fully-packed state, the pressure experienced at the interface between individual particles is equal to that within the particles. To investigate the sensitivity of the computed results to this parameter, alternate values of 1.0 and 0.5 are chosen. Setting the value to 1.0 assumes that the pressure felt at the interface between particles is only equal to the pressure inside the particles when all voids are removed from the flow. While setting the value to 0.5 implies that this same phenomena occurs at volume fractions somewhat below the fully-packed state.

The numerical results are plotted against the experimental data in Fig. 5.7. Almost no variation is detected in the results for shock motion or peak pressure. This is because the parameters being investigated only directly affect the dispersed

phase, any effect on the continuous phase, which these results are indicative of, occurs only through the variation of phase interaction resulting from any changes in particle motion. Differences are observed, however, in the plot of particle front location. Here, setting  $\alpha_{max} = 1.0$  results in a decrease in the particle front velocity. This trend may be expected because an increase in  $\alpha_{max}$  over the baseline value results in a reduction in the magnitude of  $P_D$  applied as the charge detonates. The results observed for the case in which  $\alpha_{max} = 0.5$  show little if any difference from those obtained with the baseline value of 0.62. The likely reason for this is that while setting  $P_D = 0.5$  increases the range of volume fractions over which the maximum pressure, defined by  $P_D = P_{int,D}$ , is felt, it does not increase the magnitude of the maximum pressure. Overall, these results do indicate some sensitivity of the computational results to the value of  $\alpha_{max}$  selected. By comparing the results with experiment, it is observed that setting  $\alpha_{max} = 1.0$  produces results furthest from the experiment, suggesting that this choice is not physically accurate. Additionally, because it is difficult to conceptually justify the setting  $\alpha_{max}$  significantly lower than the fully-packed state, and because doing so did not produce any quantifiable increase in accuracy, it can be loosely concluded that the assignment of  $\alpha_{max}$  to the fully-packed volume fraction is physically realistic.

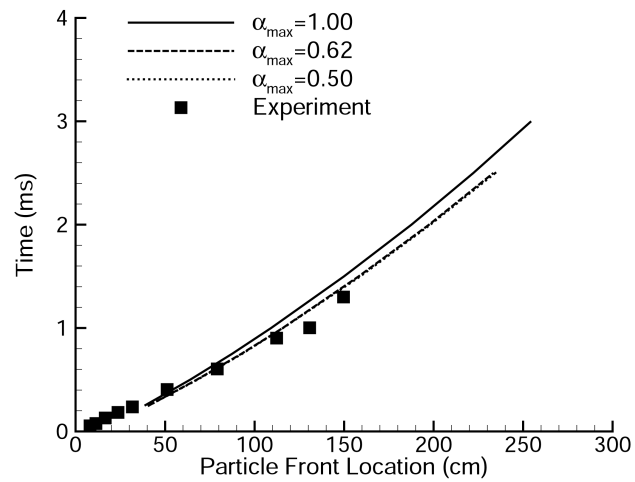
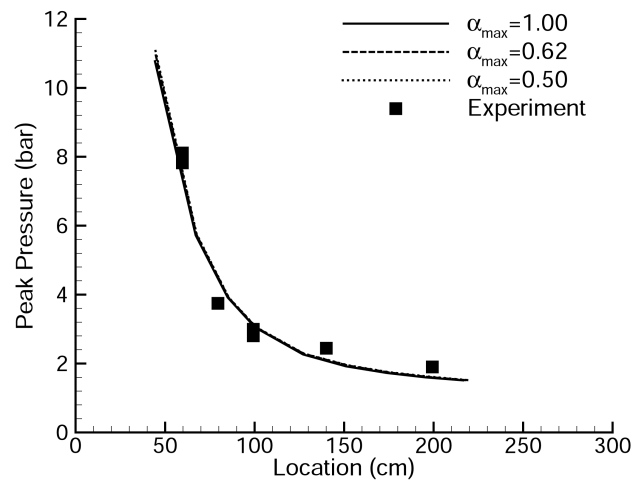
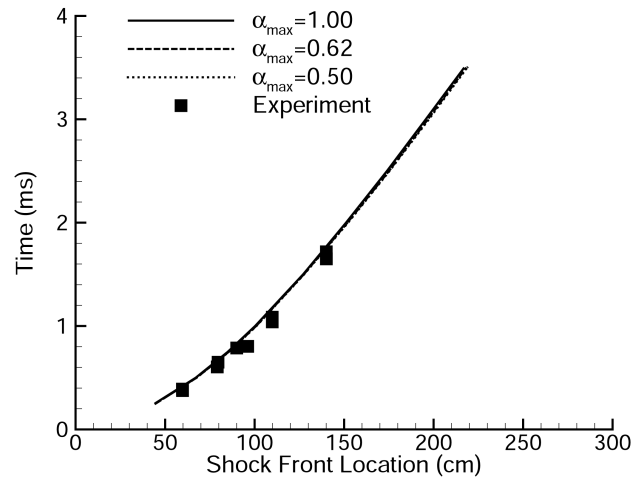


Figure 5.7: Effect of  $\alpha_{max}$  on shock propagation, peak pressure, and particle front location.

### Sensitivity to $\alpha_{min}$

Next, the effects of varying  $\alpha_{min}$  are investigated. In the same way that  $\alpha_{max}$  defines the upper limit of the transition regime for dispersed phase pressure,  $\alpha_{min}$  defines the lower limit. For  $\alpha_D \leq \alpha_{min}$ ,  $\zeta = 0$  and  $P_D$  ceases to exist. This implies that particle-particle interactions are no longer important below  $\alpha_{min}$ . The baseline value used previously was  $\alpha_{min} = 0.2$ , at this state the minimum distance between particles is approximately one particle radius if a body centered cubic structure is assumed. To investigate the sensitivity of the calculated results to this parameter, alternate values of 0.4 and 0.01 were chosen.

The numerical results are plotted against the experimental data in Fig. 5.8. Again, almost no discernible variation exists in the plots of shock trajectory and peak pressure. More surprisingly, however, little variation is observed in the plot of particle front location. The results for  $\alpha_{min} = 0.2$  & 0.4 are indistinguishable, while the results for  $\alpha_{min} = 0.01$  show a small reduction in the particle front velocity. The results indicate a general insensitivity to  $\alpha_{min}$  over the range of values investigated. Although it is noted that the larger values of 0.2 and 0.4, which are  $O(10^{-1})$ , produce *slightly* better results than the value of 0.01, which is  $O(10^{-2})$ , when compared to the experiment.

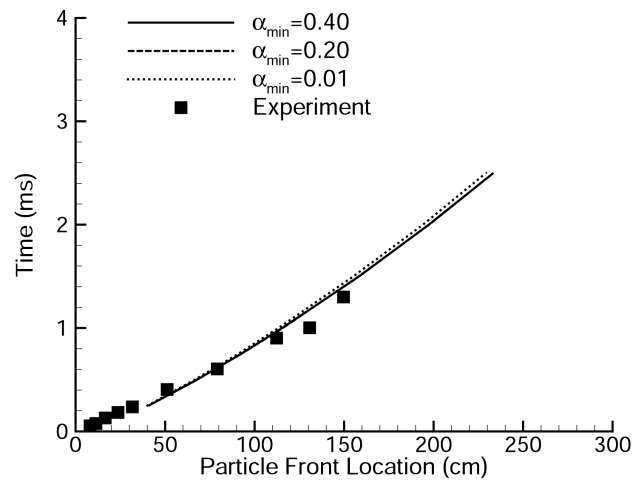
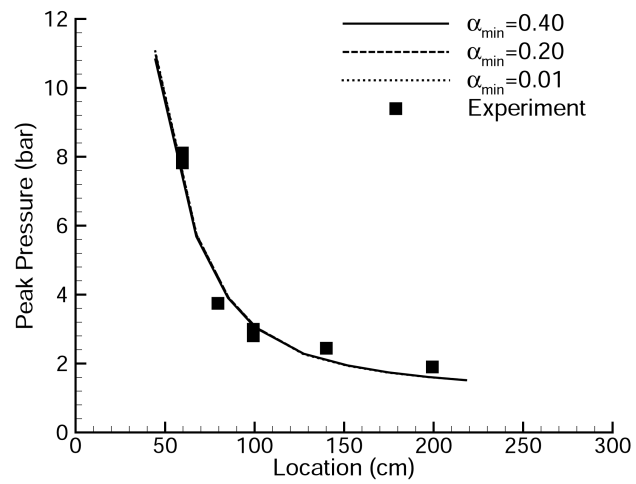
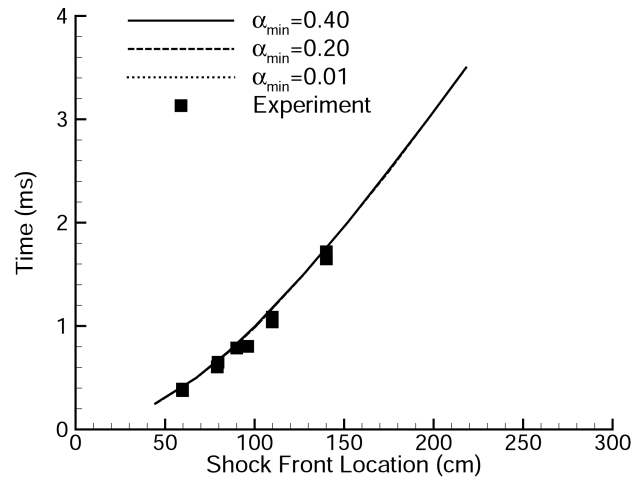


Figure 5.8: Effect of  $\alpha_{min}$  on shock propagation, peak pressure, and particle front location.

## Sensitivity to $z$

Finally, the sensitivity of the results to the parameter  $z$  are investigated. This parameter defines the shape of  $P_D$  through the transition region. In addition to the baseline value of  $z = 1$ , alternate values of 0.5 and 2 are selected. The results of the simulations are shown in Fig. 5.9. As in the previous comparisons, no effect on either the shock trajectory or peak pressure is observed. In terms of particle front motion, little variation exists between the results for  $z = 1$  & 2. Setting  $z = 0.5$ , however, causes the particle front velocity to be decreased. The result of setting  $z < 1$  is that the shape of  $\zeta$  becomes concave; this increases the slope of the curve near  $\alpha_{min}$  and decreases it near  $\alpha_{max}$ . This is notable in the context of the results obtained in the study of  $\alpha_{min}$ . In that study, decreasing  $\alpha_{min}$  to 0.01 had the effect of reducing the particle front velocity, just as setting  $z = 0.5$  does here. The interesting point is that both decreasing  $\alpha_{min}$  and increasing  $z$  have the effect of reducing the slope of  $\zeta$  near  $\alpha_{max}$ , and both make the comparison with experiment worse. This suggests that properly predicting the slope of  $\zeta$  near  $\alpha_{max}$  may be important to the correct prediction of particle motion, and that a steeper slope is more physically correct. More study is needed to confirm this analysis, but the suggested phenomenology is interesting nevertheless.

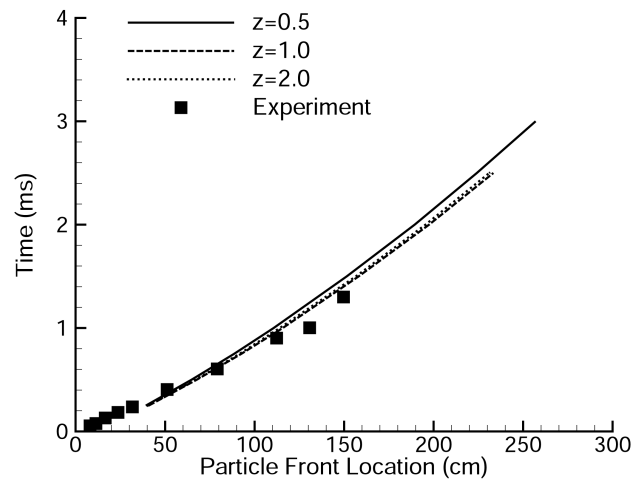
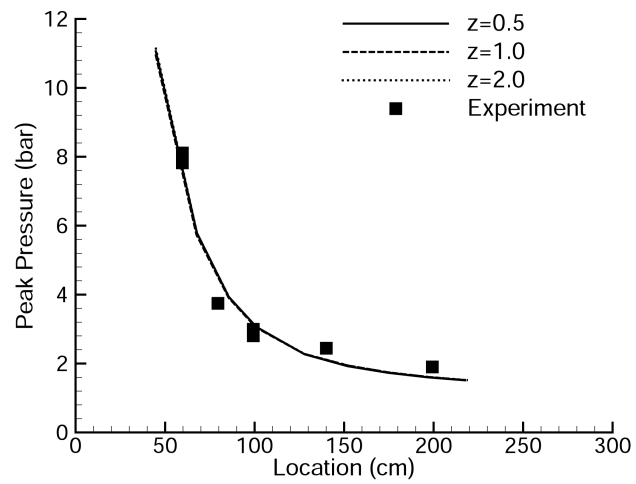
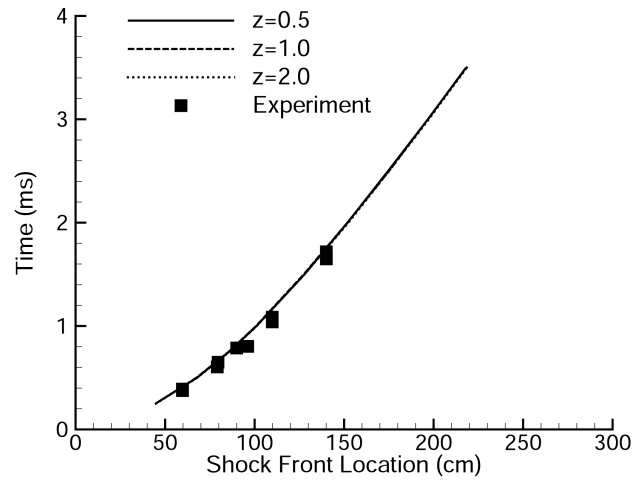


Figure 5.9: Effect of  $z$  on shock propagation, peak pressure, and particle front location.

## Chapter 6

# Effect of Physical Parameters on Multiphase Explosions

In this chapter, the effects of three physical parameters on the dynamics of multiphase explosions are investigated. The parameters considered are: particle loading, particle size, and particle material. Understanding the effects of these parameters is critical to design efforts utilizing multiphase explosion or energetic technologies. Many such applications involve reactive particles, which are intended to burn either within the detonation products or external atmosphere. In these systems, particle motion and placement are critical to obtaining the desired reactivity. While reaction rate considerations often drive the selection of key parameters such as particle size and material, it is equally important to consider the effects of these parameters on the overall explosion dynamics, including the location of the particles with respect to the shock and detonation product fronts. The location of the particles with respect to these fronts defines the oxidizer content and thermodynamic state of the media surrounding the particles, which affects the rate of reaction. While the modeling of systems containing reactive particles is important, the current work investigates explosives containing inert particles. The use of inert particles allows for a simpler analysis that focuses exclusively on explosion dynam-

ics and is not complicated by the effects of reaction. It also avoids the complexities surrounding the modeling of burning particles, which is a major research topic in and of itself. Nevertheless, the results of this study provide fundamental insight into the effects of particle loading, size, and material on multiphase explosion dynamics, an understanding of which is critical in the analysis of systems containing either inert or reactive particles.

The baseline configuration of the explosive considered in this study is again taken from the experiments of Zhang et al. [32]. The charge is an 11.8 *cm* diameter sphere containing sensitized nitromethane and spherical solid particles. It is suspended in air and centrally detonated, allowing for the use of a 1-D model. In Ch. 4 and Ch. 5 numerical simulations based directly on this experiment were used to validate the numerical model and investigate the sensitivities of the computed results to various modeling correlations. The studies performed in this chapter are no longer intended to directly simulate the experiments; however, the baseline charge configuration is retained because it is relatively simple and computationally efficient to employ in the context of a parametric study.

## 6.1 Effect of Particle Loading

First, the effect of initial particle loading is investigated. The original experiments [32] contained a fully-packed bed of 463  $\mu m$  steel particles, resulting in an initial particle loading of 62% by volume ( $\alpha_D = 0.62$ ). In this section, 463  $\mu m$  steel particles are again used, but the initial particle loading is varied. The particle loadings investigated are listed in Tab. 6.1 in terms of both volume and mass fraction. The entire range of possible loadings is investigated, from zero particles to the fully-packed state. In the numerical simulations, all parameters except the initial particle loadings were held constant.

Particle volume fraction ( $\alpha_D$ )	0.0	0.15	0.30	0.62
Particle mass fraction ( $Y_D$ )	0.0	0.55	0.75	0.92

Table 6.1: Particle volume and mass fractions investigated in Sec. 6.1

Results from the numerical simulations are summarized in Figs. 6.1-6.4. The results include the shock, particle, and detonation front trajectories, as well as the peak pressures calculated for all four initial particle loadings. From these figures, it is observed that decreasing the initial particle volume fraction increases the shock front velocity, peak pressure, particle front velocity, and detonation product front velocity. It is also observed that the maximum radius of the detonation product front (also called the fireball) is increased as the particle volume fraction is decreased. Two factors account for these trends. First, because the particles displace volume that would otherwise be occupied by nitromethane, the total explosive mass and energy increase as the particle loading decreases. Thus there is simply more energy available in systems with lower particle content. Secondly, the particles act as sinks to the surrounding explosive. The drag force that accelerates the particles is felt equally and oppositely by the surrounding media, which restricts the outward flow during the initial phase of the explosion. In the same way, the heat transferred from the detonation products to the particles removes energy from the explosive gas that would otherwise be available to do work. Thus in addition to having a reduced amount of explosive mass and energy, the configurations with higher particle loadings are further restricted by dissipative losses resulting from the phase interactions.

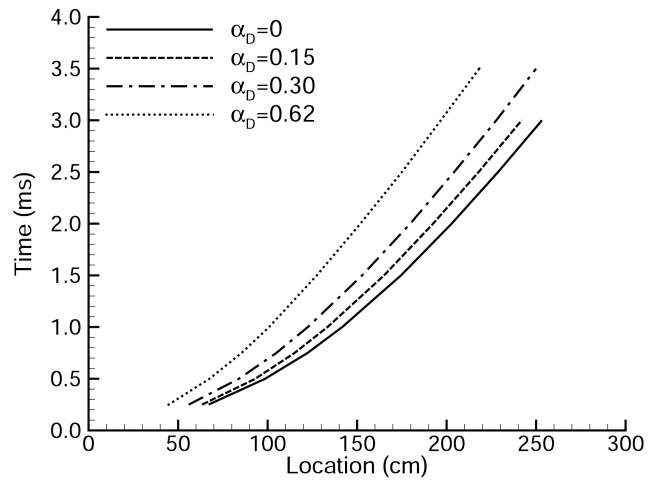


Figure 6.1: Effect of initial particle loading on shock front motion.

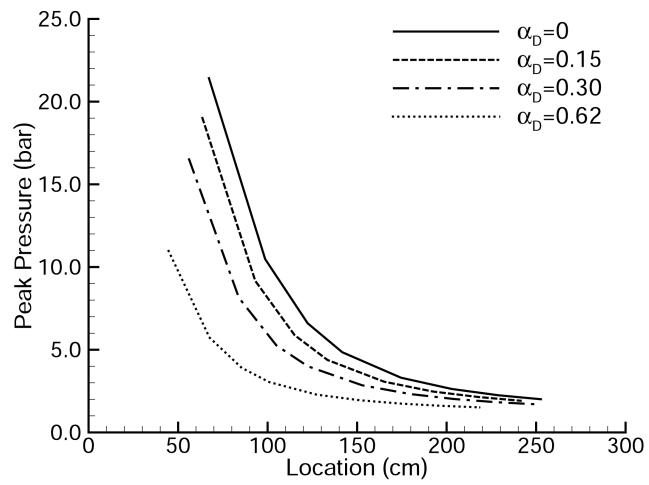


Figure 6.2: Effect of initial particle loading on peak pressure.

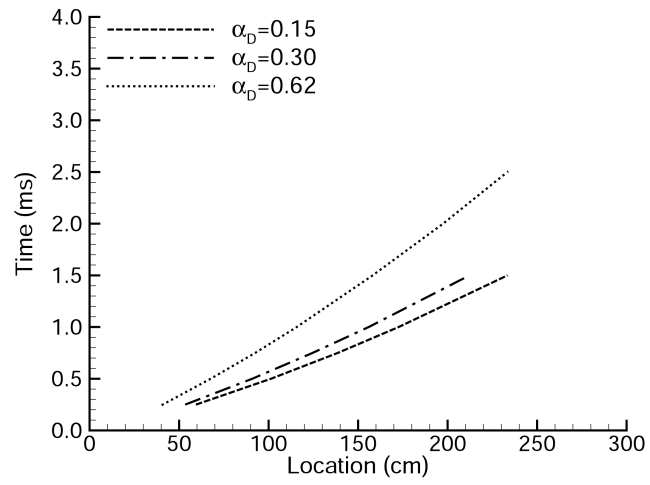


Figure 6.3: Effect of initial particle loading on particle front motion.

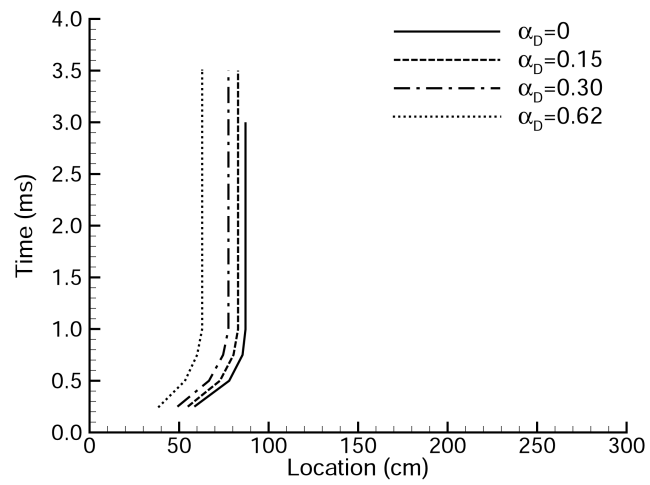


Figure 6.4: Effect of initial particle loading on detonation product front motion.

The effects of initial particle loading are illustrated in more detail in Figs. 6.5 and 6.6, which contain spatial profiles of volume fraction and velocity at 0.25 and 1.0 *ms* after detonation. Results are only shown here for the charges initially containing 15% particles by volume; the corresponding results with 62% particle loading were shown previously in Figs. 4.1 and 4.3. When comparing the plots at equivalent times, it is easily observed that the increasing the initial particle loading has resulted in significant damping of the velocities for both the continuous and dispersed phases. At 0.25 *ms* the peak velocity in the dispersed phase is above  $1.5 \times 10^5$  *cm/s* for the 15% steel charge, while below  $1.0 \times 10^5$  *cm/s* for the 62% steel charge. This trend in velocities continues through 1.0 *ms*, where the 15% steel charge has produced substantially more separation between the particle and shock fronts than the 62% steel charge. Although there are fewer total particles in the 15% steel charge, they have propagated further into the ambient, pre-shock environment in this time-frame. The smaller initial volume fraction, along with the increased particle velocity, has also resulted in a volume fraction profile that is generally lower in magnitude and more spread out in the case of 15% particle loading when compared to 62%.

One more interesting point comes out of this comparison. In Ch. 5, a detailed analysis of the effects of dispersed phase pressure was presented. Results of this analysis demonstrated the importance of the dispersed phase pressure  $P_D$  to the accurate prediction of the particle front motion. In the case of a fully-packed particle bed, it was shown that neglecting the  $P_D$  resulted in the under-prediction of the particle front velocity. Because it is a function of volume fraction,  $P_D$  is only active when  $\alpha_D \geq \alpha_{min}$ ; where from Sec. 5.3,  $\alpha_{min} = 0.2$  was shown to be reasonable. Hence in the current simulations, the force due to a dispersed phase pressure gradient is only active in the simulations with 30% and 60% initial particle loadings by volume. Thus, these scenarios are to some extent subject to

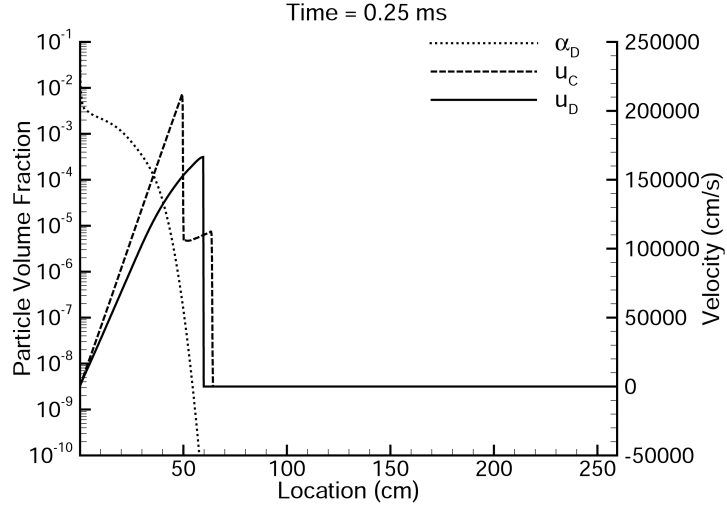


Figure 6.5: Velocity and volume fraction profiles at 0.25 *ms* for explosion of nitromethane charge with 463  $\mu\text{m}$  steel particles; 15% initial particle loading by volume.

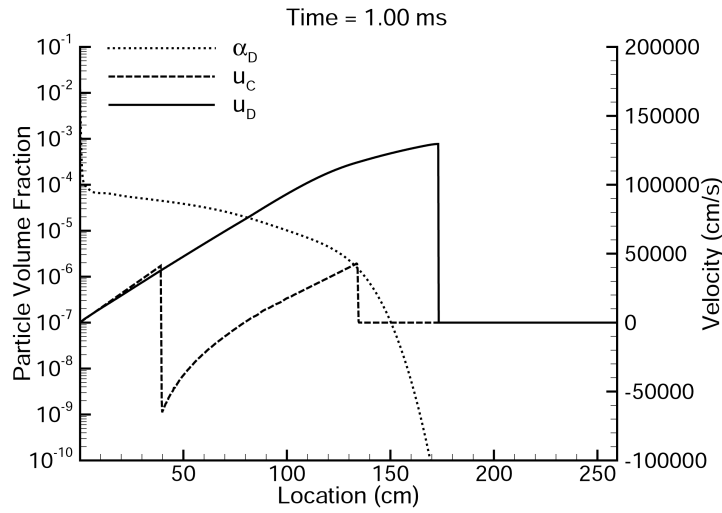


Figure 6.6: Velocity and volume fraction profiles at 1.00 *ms* for explosion of nitromethane charge with 463  $\mu\text{m}$  steel particles; 15% initial particle loading by volume.

an extra force not active in simulations with lower initial loadings. The interesting point is that despite the presence of the pressure gradient force, the particle front velocities for the 30% and 62% particle loadings still fall well below that observed for the 15% particle loading. This indicates that the increased explosive energy in the systems with lower particle loadings coupled with the decreased total mass of particles results in particle accelerations that are greater than those in systems with higher particle loadings, despite the lack of a pressure gradient force.

## 6.2 Effect of Particle Diameter

In this section, the influence of particle size is investigated. The explosive configuration uses steel particles at a fixed initial loading of 62% particles by volume. Two particle sizes are then considered: 463  $\mu m$  and 46.3  $\mu m$ . The former aligns with the baseline particle size from the experiment [32], while the latter is an order of magnitude smaller. After these configurations are analyzed, results are presented for the same scenario but with an initial particle loading of 15% by volume.

Figs. 6.7 and 6.8 present the shock, particle, and detonation product front trajectories for the charges with 46.3  $\mu m$  and 463  $\mu m$  particles, respectively. It is immediately observed that reducing the particle size by an order of magnitude significantly alters the explosion dynamics. The most obvious change relates to the ability of the particles to escape and out-run the shock. When 463  $\mu m$  particles are used, the leading particle front escapes the shock at approximately 0.5  $ms$  and continues to separate from it in the time-frame considered. The 46.3  $\mu m$  particles escape the leading shock more rapidly; the particle front leads the shock front at 0.25  $ms$ , which was the earliest time recorded in the simulation. However, after the initial escape, the 46.3  $\mu m$  particle front fails to continue separating from the shock. Rather, the trajectories of the two fronts become somewhat parallel initially before beginning to converge at 1  $ms$ . The waves come together between 2.8-3.0  $ms$ , at which time the shock overtakes and begins to separate from the particle front.

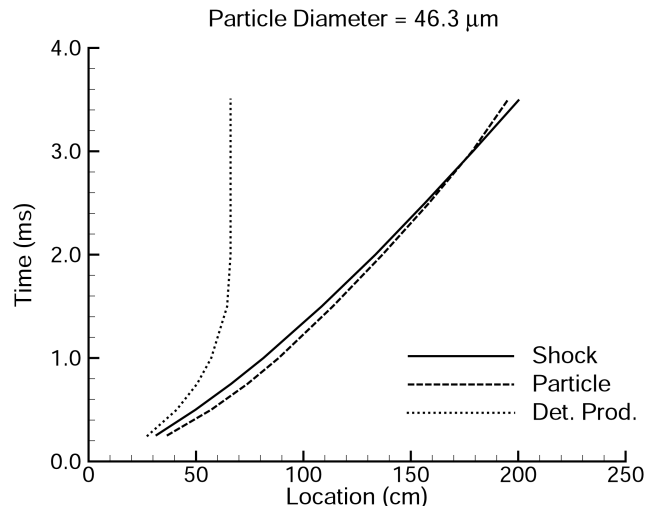


Figure 6.7: Shock, particle, and detonation front trajectories from nitromethane charge with 46.3  $\mu\text{m}$  steel particles; 62% particles by volume.

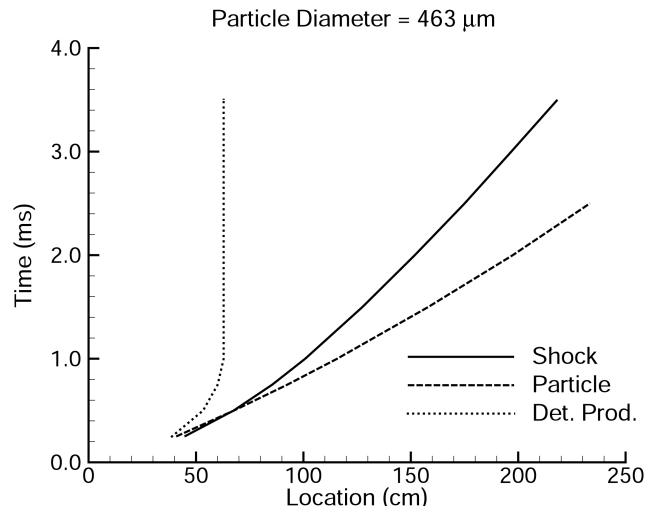


Figure 6.8: Shock, particle, and detonation front trajectories from nitromethane charge with 463  $\mu\text{m}$  steel particles; 62% particles by volume.

Spatial profiles of the explosion containing  $46.3 \mu\text{m}$  particles are shown in Figs. 6.9 and 6.10. The plots contain the phase velocities along with the dispersed phase volume fraction at 0.5 and 2.0  $\text{ms}$ . The corresponding results for the  $463 \mu\text{m}$  particles are shown in Figs. 4.2 and 4.4. Comparing the results at 0.5  $\text{ms}$ , it is immediately observed that the velocity profiles for both phases are shaped somewhat differently for the two particle sizes, and that the velocities are lower for the case with  $46.3 \mu\text{m}$  particles. At 2.0  $\text{ms}$ , the  $46.3 \mu\text{m}$  particle front has progressed only about 140  $\text{cm}$  into the domain, and is closely aligned with the shock front. Conversely, the  $463 \mu\text{m}$  particles have progressed further into the domain; the particle front is nearing 200  $\text{cm}$ , while the shock front trails at about 150  $\text{cm}$ .

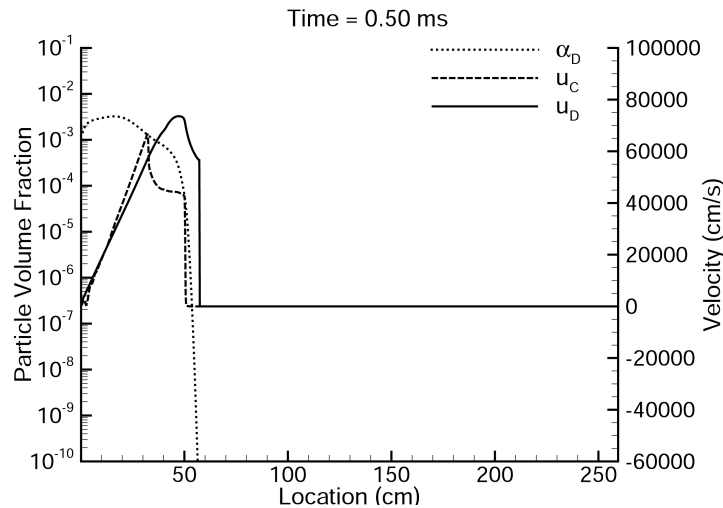


Figure 6.9: Velocity and volume fraction profiles at 0.50  $\text{ms}$  for explosion of nitromethane charge with  $46.3 \mu\text{m}$  steel particles; 62% initial particle loading by volume.

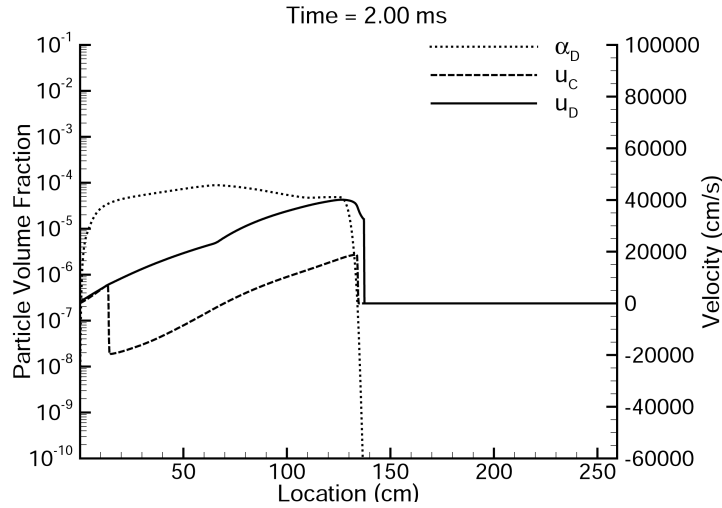


Figure 6.10: Velocity and volume fraction profiles at 2.00 *ms* for explosion of nitromethane charge with 46.3  $\mu\text{m}$  steel particles; 62% initial particle loading by volume.

From these results, it is clear that significant differences in the explosion dynamics exist. Throughout the time-frame considered, the charge containing 463  $\mu\text{m}$  particles produces higher velocities for both the continuous and dispersed phases than does the charge with 46.3  $\mu\text{m}$  particles. Yet the 46.3  $\mu\text{m}$  particles escape the leading shock earlier in time, meaning that initially the relative velocity of the 46.3  $\mu\text{m}$  particle front with respect to the shock is higher than that of the 463  $\mu\text{m}$  particle front. These results may at first seem inconsistent given that both were produced by charges with exactly the same explosive and particle mass. However, the differences observed are completely explained by dissipation among the phases.

To understand how dissipation among the phases can so drastically effect the explosion dynamics, consider the effects of particle diameter on the drag force and heat transfer rate. The drag force is defined by Eq. (3.27). Neglecting Mach number effects, the drag force per unit volume  $f$  scales with diameter as:

$f \propto DC_d N$ . Assuming  $Re \geq 1000$ ,  $C_d \propto D$ . Additionally,  $N \propto D^{-3}$ . This leaves  $f \propto D^{-1}$ . Thus reducing the particle diameter by an order of magnitude results in approximately a 10X increase in the drag force. A similar effect occurs with the heat transfer rate, defined in Eq. (3.29). Here  $\dot{q} \propto DNuN$ . Again assuming high Reynolds number  $Nu \propto Re^{1.5} \propto D^{1.5}$ . This results in  $\dot{q} \propto D^{-1.5}$ , so that reducing the particle diameter by 10 results in approximately a 31X increase in the heat transfer rate.

This simple analysis clearly shows that decreasing the particle diameter increases the magnitude of the drag and heat transfer, which results in an overall increase in the rate of dissipation among the phases. This directly explains the results observed. In the charge with 46.3  $\mu m$  particles, the increased drag force accelerates the particles more quickly, and slows the surrounding media, resulting in a reduced time for the particles to escape the shock. The increased drag force also increases the rate of waste heat generation, which in combination with the increased heat transfer rate, reduces the amount of energy available to do work. This is confirmed in Figs. 6.11 and 6.12, which compare the temperatures of the 46.3 and 463  $\mu m$  particles at 0.50 and 2.00  $ms$ . The 46.3  $\mu m$  particles have temperatures 100-300  $K$  higher than the 463  $\mu m$  particles at equivalent times. Recalling that the particles make up 92% of the initial mass of the charge, it is clear that a significant amount of energy was required obtain this extra temperature rise. It is the loss of this energy that creates the disparity in the explosion dynamics observed with the different particle sizes. The energy lost through increased dissipation in the system containing the smaller particles is apparent not only in the decreased phase velocities, but also in the pressure. Fig. 6.13 shows the peak pressures observed at different ranges from the charge. As would be expected from the preceding analysis, the pressures generated by the charge with 46.3  $\mu m$  particles are damped with respect to those obtained with the 463  $\mu m$  particles.

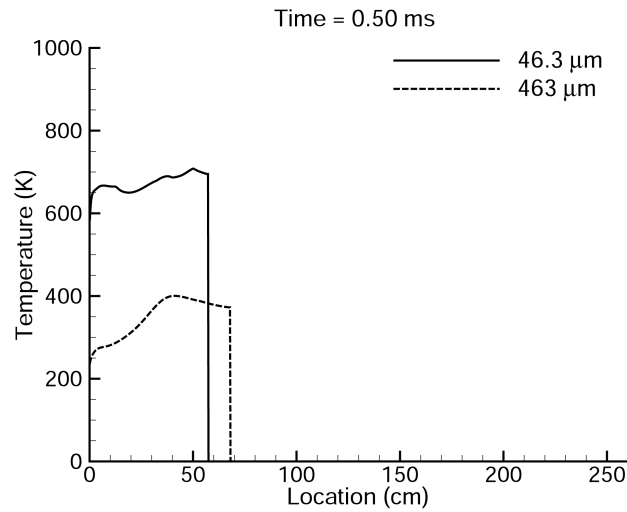


Figure 6.11: Temperature profiles at 0.50 *ms* for explosions of nitromethane charges with 46.3 and 463  $\mu\text{m}$  steel particles; 62% initial particle loading by volume.

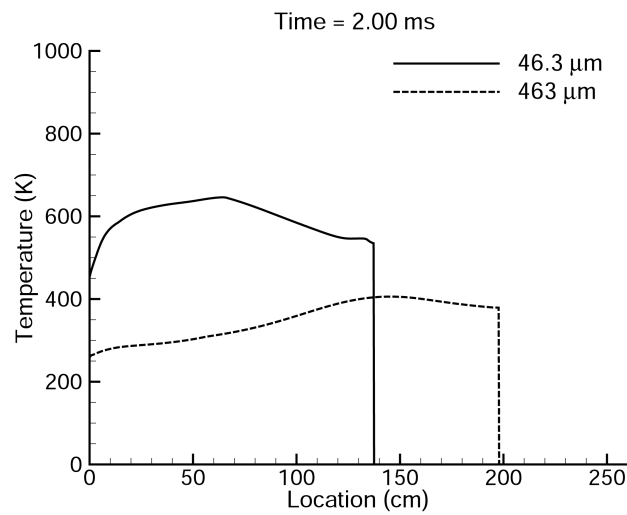


Figure 6.12: Temperature profiles at 2.00 *ms* for explosions of nitromethane charges with 46.3 and 463  $\mu\text{m}$  steel particles; 62% initial particle loading by volume.

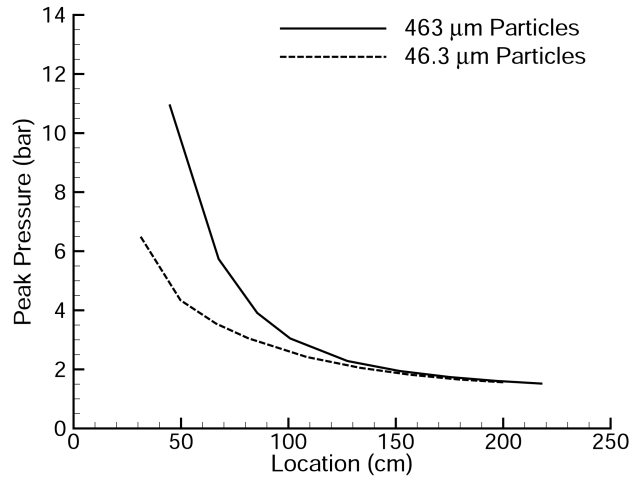


Figure 6.13: Peak shock pressures from explosions of nitromethane charges with 46.3 and 463  $\mu m$  steel particles; 62% initial particle loading by volume.

From the results presented, it is clear that particle size can significantly effect multiphase explosion dynamics. Given the rather large reductions in pressure and velocities that have been observed, and because the initial particle loadings of the charges considered were high (62% by volume), it is natural to ask whether such an effect is observed in systems with lesser particle loadings. Results from simulations identical to those above, but using charges with only 15% particles by volume are presented in Figs. 6.14 and 6.15. These figures plot the shock, particle, and detonation product front trajectories. The trends among the particle sizes are identical to those for the charges with 62% particles. Hence it is observed that the increased dissipation among phases affects these more lightly-loaded charges in much the same way as it affected the fully-packed charges.

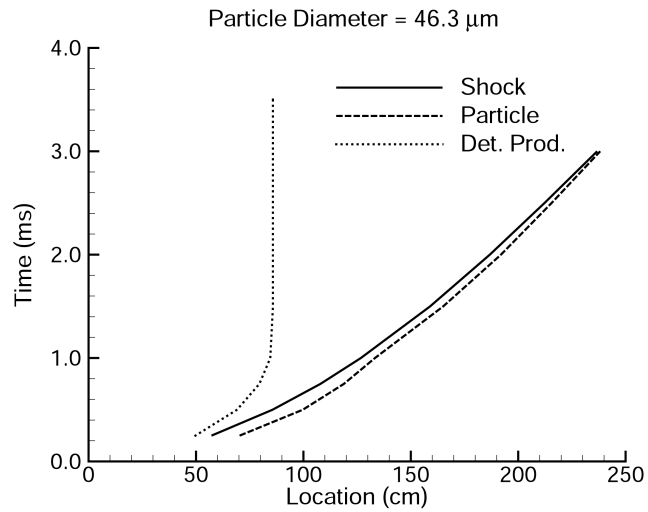


Figure 6.14: Shock, particle, and detonation front trajectories from nitromethane charge with 46.3  $\mu\text{m}$  steel particles; 15% initial particle loading by volume.

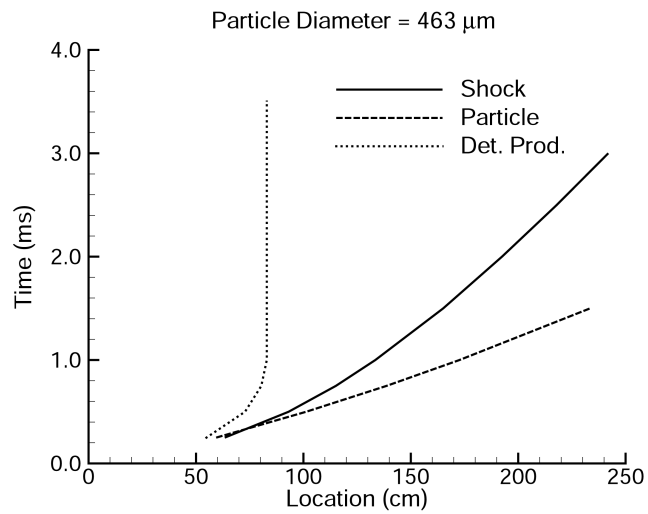


Figure 6.15: Shock, particle, and detonation front trajectories from nitromethane charge with 463  $\mu\text{m}$  steel particles; 15% initial particle loading by volume.

### 6.3 Effect of Particle Material

In this section, the influence of particle material is investigated. Steel and soda-lime glass particles are considered. The properties of both the steel and glass particles at ambient conditions are given in Tab. 6.2. The glass is approximately 3X less dense than steel, is slightly more compressible, and has a smaller heat capacity. The initial particle loading and particle diameter are held constant in this study, and are taken as 62% by volume and 463  $\mu m$ , respectively.

Material	Density( $g/cc$ )	Sound Speed( $cm/s$ )	Heat Capacity( $c_v$ ) ( $erg/g/K$ )
Steel	7.795	$4.44 \times 10^5$	$4.46 \times 10^6$
Glass	2.5	$4.09 \times 10^5$	$1.60 \times 10^6$

Table 6.2: Particle material properties

The trajectories of the shock, particle and detonation product fronts for the charge containing glass particles are plotted in Fig. 6.16. The corresponding plot for the steel particles was previously shown in Fig. 6.8. Because the glass particles are lighter, they are accelerated more rapidly than the steel particles, and are less restrictive to the surrounding flow. The glass particles therefore achieve higher velocities and escape the shock front at an earlier time. The glass particle front passes the leading shock sometime prior to 0.25  $ms$ , while the steel particle front does not pass the shock until 0.5  $ms$ . The detonation product front also achieves a larger radius when glass particles are used, although the difference is slight.

The peak pressures generated by the two charges are compared in Fig. 6.17. The pressures are higher for the charge with the glass particles, which is consistent with the higher shock velocity. This is again caused by the decreased resistance the glass particles exert on the surrounding flow, which generates less waste heat and increases the energy available to do work.

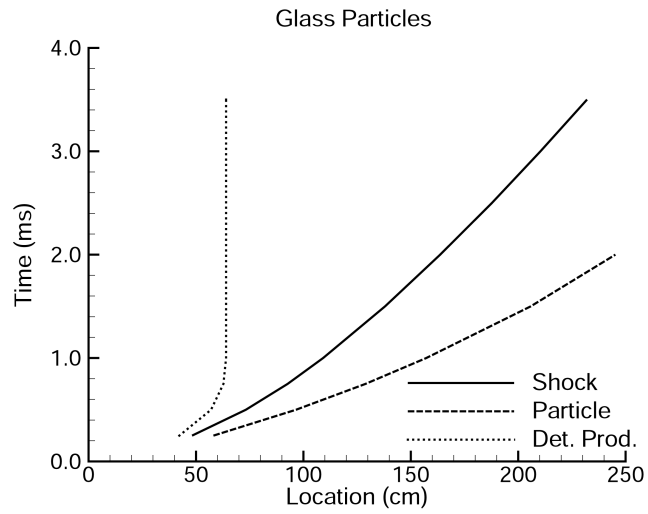


Figure 6.16: Shock, particle, and detonation front trajectories from nitromethane charge with  $463 \mu\text{m}$  glass particles; 62% initial particle loading by volume.

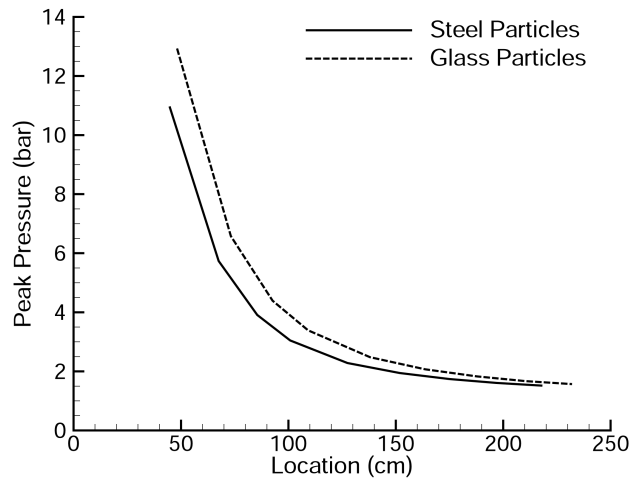


Figure 6.17: Peak pressures from nitromethane charges with  $463 \mu\text{m}$  steel or glass particles; 62% initial particle loading by volume.

Profiles of the phase velocities and particle volume fractions for the charge containing glass particles are shown in Figs. 6.18 and 6.19. The results are plotted at both 0.5 and 2.0 *ms*. The steel particle results are shown in Figs. 4.2 and 4.4. From these plots, the difference in particle velocities are apparent. By 2.0 *ms*, the glass particle front is located between 240-250 *cm*, and is nearing the edge of the computational domain. The steel particles trail significantly, having not yet reached 200 *cm* at the same time. Although lighter, the glass particles are still able to run-away from the shock. It is also interesting to compare the shapes of the particle velocity profiles between the two materials. In the case of steel particles, the discontinuous rise at the particle front is followed by a smooth and monotonic decrease to zero at the origin. The profiles for the glass particles are similar but do not monotonically decay. At 0.5 *ms* the discontinuous rise at the particle front is followed by smooth rise that continues to the location of the shock front, while at 2.0 *ms* a peak in the particle velocity is also observed at the location of the shock. These results indicate that once initially accelerated, the steel particles are less affected by the surrounding flow than are the glass particles, which is another consequence of the material density difference.

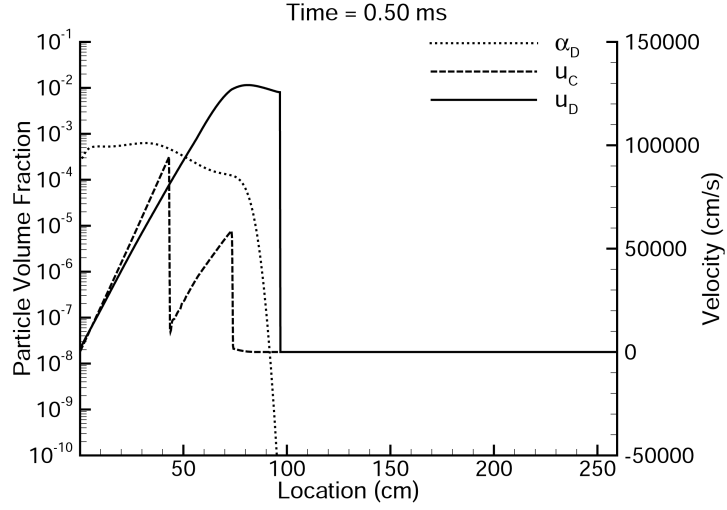


Figure 6.18: Velocity and volume fraction profiles at 0.50 *ms* for explosion of nitromethane charge with 463  $\mu\text{m}$  glass particles; 62% initial particle loading by volume.

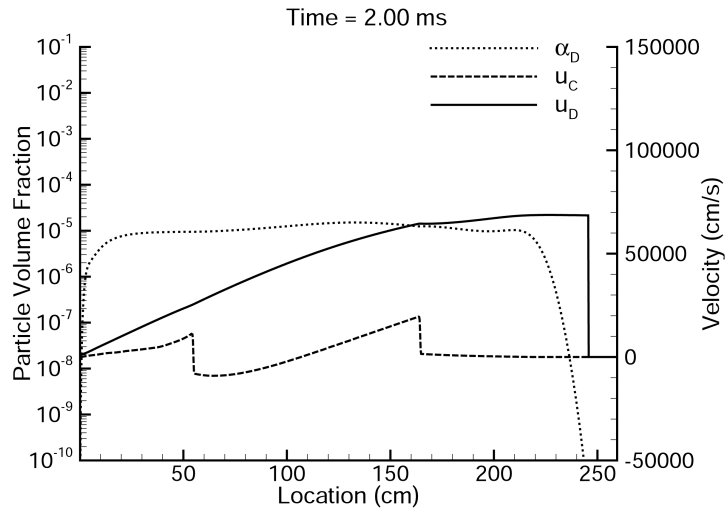


Figure 6.19: Velocity and volume fraction profiles at 2.00 *ms* for explosion of nitromethane charge with 463  $\mu\text{m}$  glass particles; 62% initial particle loading by volume.

## Chapter 7

### Conclusions and Future Work

In this research, a compressible multiphase flow model for the numerical simulation of multiphase explosions has been proposed, developed, and applied. The model development effort was motivated by the lack of a satisfactory numerical technique in the literature. While numerous related models have been proposed, none are completely satisfactory. Sources of contention include the governing equations, representations of dispersed materials, treatment of phase compressibility and non-equilibrium effects, and the numerical schemes applied. The model developed in this work distinguishes itself from others in the literature by: 1) treating all phases as fully compressible, 2) properly representing the mathematical characteristics of dispersed particle phases in the both the dense and dilute limits, 3) applying a Godunov-based solution to all phases, and 4) allowing complete non-equilibrium among phases. In application, the model has been shown to produce results that compare well with existing experimental data. Additional studies have investigated the sensitivity of the numerical model to correlations for drag, heat transfer, and dispersed phase pressure, as well as to physical parameters including particle loading, size, and material.

To develop a numerical model for multiphase explosions, the governing equations for a compressible multiphase flow were first derived and discussed. The

derivation revealed the physical origins of the terms in the governing equations, and provided a basis for the discussion of the nozzling terms, which are a source of debate in the literature. A discussion of the physical nature of dispersed materials was also presented, and a generic equation of state including a functional dependence on volume fraction was proposed. A characteristic analysis of the governing equations (presented in the appendix) was also performed and discussed. The mathematical characteristics of the governing equations were shown to be hyperbolic and the characteristic equations later used in the Riemann solver development were derived.

The numerical solution to the governing equations is based on a time- and dimensionally-split finite volume method. Time-splitting was used to separate the governing equations into convective and source terms, which are solved independently. Dimensional-splitting allows the extension of a 1-D solver to systems of higher dimension. An original contribution of this work was the development of the multiphase Riemann solver, which forms the basis of a Godunov-type solution to the convective portion of the governing equations. The Riemann solver was developed from the characteristic relations derived in the appendix. The solution technique is approximate, non-iterative, and decoupled among phases. It is also applicable to both continuous and dispersed phase materials because it was derived under the assumption of a generic equation of state. To properly represent the mathematical characteristics of a dispersed materials, a dispersed phase equation of state with a functional dependence on volume fraction was proposed. The proposed equation of state, along with the study of dispersed phase pressures performed in Ch. 5, represent a second original contribution to the literature.

Results from numerical calculations were compared with existing experimental data to demonstrate the validity of the modeling approach developed. Comparisons with two experiments were presented, Both scenarios involved the detonation

of a multiphase charge consisting of a dispersed collection of particles embedded in an explosive fill. The comparisons also covered a range of initial particle loadings, from a fully-packed bed with 62% particles by volume, to a more lightly loaded scenario with only 10% particles by volume. Results available for comparison included transient shock and particle front motion, pressure gauge data, and fast-framing camera images. Numerical calculation results were shown to compare well with the experimental data, providing confidence in the numerical method.

The sensitivities of the numerical results to the chosen correlations for drag, heat transfer, and dispersed phase pressure were then investigated. A comparison of the computational results to experimental data revealed the sensitivities of the model to the chosen correlations, and provided fundamental information on the modeling techniques most accurately addressing the physics of the flow. In the investigation of drag correlations, the results indicate that accounting for the volume fraction dependence on the drag force is necessary to obtaining accurate predictions. From the study of heat transfer, the comparison with experiment suggested that the baseline heat transfer rate was sufficient to produce accurate results. Perhaps the most important conclusion comes from the study of dispersed phase pressure. Here, various methods of representing the dispersed phase pressure, including using the proposed dispersed phase equation of state, were investigated. By comparing the results with experimental data, it was shown that accounting for the volume fraction dependence on the dispersed phase pressure is critical to obtaining accurate predictions of particle motion. An analysis of the physics driving this conclusion showed that this result is a function of the transition of the mathematical characteristics of the dispersed phase from fully-hyperbolic to hyperbolically degenerate within the time-frame of the event. This transition leads to the negation of the dispersed phase pressure gradient in the time-frame where it would serve to restrict the particle flow. This phenomena is a direct consequence

of the dependence of dispersed phase pressure on volume fraction. This result confirms the physical nature of dispersed materials discussed in this work, as well as the dispersed phase equation of state proposed.

Finally, the numerical model was used to investigate the effects of physical parameters on multiphase explosion dynamics. While only inert particles were considered in this study, the results of this analysis are important for understanding the behavior of systems utilizing reactive particles, as the particle motion defines the oxidizer content and thermodynamic state the particles see. From the simulations performed, several trends were observed. First, decreasing the initial particle loading in a multiphase explosive serves to increase the shock, particle, and detonation front velocities, as well as the peak pressures. The maximum size of the fireball also increased when the initial particle content was decreased. This trend is driven primarily by the increase in explosive mass and decrease in dissipation obtained with lighter particle loadings. Next, an analysis of the effects of particle diameter showed that decreasing the particle diameter results in increased dissipation among the phases. When the particle diameter was decreased by an order of magnitude, the increased dissipation rate significantly altered the explosion dynamics. While the temperature of the particles was increased, the velocities of both phases were substantially decreased when the smaller particle size was used. This had the overall effect of inhibiting the ability of the particles to run-away from the leading shock into the ambient atmosphere. Finally, in an investigation of particle material effects, computations indicated that using lighter particles results in increased velocities of the shock and detonation fronts, along with an increase in the pressure generated. This trend occurs because lighter particles require less force to accelerate, allowing them to obtain higher velocities and providing less resistance to the surrounding flow.

The current work has provided a strong theoretical and computational ba-

sis for the investigation of compressible multiphase flows containing a dispersed particle phase. However, plans to extend the utility of the model remain. In the near future, these plans include the addition of reactive particles to the numerical model. Many systems applying multiphase explosion technologies contain reactive particles, and particle combustion is a major research area. To extend the utility of the model further, plans to combine the multiphase techniques developed in this work with existing techniques for solving multifluid flows also exist. This upgrade would allow for simulations containing more than one continuous phase material, as is found in the example of a cased explosive charge.

# Appendix A

## Characteristic Analysis

This appendix contains a review of the characteristic analysis for the compressible multiphase flow equations (1-6). In accordance with the time-split solution methodology applied, only the convective portion of the multiphase equations are analyzed here Eqs. (3.2–3.6). The objective of the characteristic analysis is to linearize the governing equations in terms of primitive variables such that the eigenvalues, eigenvectors, and characteristic equations can be determined. As such, we choose the primitive variable to be  $W = (\alpha_k, N_k, v_k, P_k, u_k, \rho_k e_k)^T$ , and seek to present the equations in the form:

$$\mathbf{W}_t + \mathbf{A}\mathbf{W}_r = \mathbf{B} \quad (\text{A.1})$$

To maintain the generality of this analysis, it is desirable not to prescribe a specific equation of state. Rather, we use the chain rule expansion for a change in pressure given the generic form in Eq. (2.28):

$$dP_k = \left. \frac{\partial P_k}{\partial \alpha_k} \right|_{\rho, e} d\alpha_k + \left. \frac{\partial P_k}{\partial \rho_k} \right|_{e, \alpha} d\rho_k + \left. \frac{\partial P_k}{\partial e_k} \right|_{\rho, \alpha} de_k \quad (\text{A.2})$$

Using this relation, the governing equations are recast in terms of the primitive variables, resulting in the coefficient matrices:

$$\mathbf{A} = \begin{bmatrix} u_i & 0 & 0 & 0 & 0 & 0 \\ 0 & u_k & 0 & 0 & 0 & 0 \\ 0 & 0 & u_k & 0 & 0 & 0 \\ \frac{\rho_k}{\alpha_k} (u_k a_{s,k}^2 - u_i a_{i,k}^2) & 0 & 0 & u_k & \rho_k c_k^2 & 0 \\ \frac{(P_k - P_{s,k})}{\alpha_k \rho_k} & 0 & 0 & \frac{1}{\rho_k} & u_k & 0 \\ \frac{\rho_k}{\alpha_k} (u_k h_{s,k} - u_i h_{i,k}) & 0 & 0 & 0 & \rho_k h_k & u_k \end{bmatrix} \quad (\text{A.3})$$

$$\mathbf{B} = -\frac{n}{r} \left[ 0, N_k u_k, 0, \rho_k u_k c_{s,k}^2, \frac{(P_k - P_{s,k})}{\rho_k}, \rho_k u_k h_{s,k} \right]^T \quad (\text{A.4})$$

The eigenvalues of this system are those of matrix  $\mathbf{A}$ :

$$\begin{aligned} \lambda_i &= u_i \\ \lambda_0 &= u_k \quad (\text{multiplicity of } 3) \\ \lambda_{\pm} &= u_k \pm c_k \end{aligned} \quad (\text{A.5})$$

The left eigenvectors satisfy the equation:

$$\mathbf{l} [\lambda \mathbf{I} - \mathbf{A}] = 0 \quad (\text{A.6})$$

Using Eq. (A.6), the left eigenvectors associated with each eigenvalue are:

$$\lambda_i = u_i;$$

$$\mathbf{l}_i = [1, 0, 0, 0, 0, 0] \quad (\text{A.7})$$

$$\lambda_0 = u_k;$$

$$\mathbf{l}_0^1 = [0, 0, 1, 0, 0, 0] \quad (\text{A.8})$$

$$\mathbf{l}_0^2 = \left[ -\frac{\rho_k N_k (u_k h_{s,k} - u_i h_{i,k})}{\alpha_k (u_k - u_i)}, \rho_k h_k, 0, 0, 0, -N_k \right] \quad (\text{A.9})$$

$$\mathbf{l}_0^3 = \left[ \frac{\rho_k h_k (u_k a_{s,k}^2 - u_i a_{i,k}^2) - \rho_k c_k^2 (u_k h_{s,k} - u_i h_{i,k})}{\alpha_k (u_k - u_i)}, 0, 0, h_k, 0, -c_k^2 \right] \quad (\text{A.10})$$

$$\lambda_+ = u_k + c_k;$$

$$\mathbf{l}_+ = \left[ \frac{\rho_k (u_k a_{s,k}^2 - u_i a_{i,k}^2) + c_k (P_k - P_{s,k})}{\alpha_k (u_k - u_i + c_k)}, 0, 0, 1, \rho_k c_k, 0 \right] \quad (\text{A.11})$$

$$\lambda_- = u_k - c_k;$$

$$\mathbf{l}_- = \left[ \frac{\rho_k (u_k a_{s,k}^2 - u_i a_{i,k}^2) - c_k (P_k - P_{s,k})}{\alpha_k (u_k - u_i - c_k)}, 0, 0, 1, -\rho_k c_k, 0 \right] \quad (\text{A.12})$$

From Eqs. (A.7–A.12), the system of equations is observed to be hyperbolic, having real eigenvalues and distinct eigenvectors.

Finally, the characteristic equations are determined by multiplying Eq. (A.1) by the associated eigenvalue and eigenvector, which after simplification yields the general expression for the characteristic equations:

$$\mathbf{l} \frac{d\mathbf{W}}{dt} = \mathbf{l} \mathbf{B} \quad (\text{A.13})$$

Substituting the left eigenvectors into this equation produces the characteristic equations for the multiphase system. These equations describe the variation of the

primitive variables along the characteristics. They are:

$$\begin{aligned}\lambda_i &= u_i; \\ \frac{d\alpha_k}{dt} &= 0\end{aligned}\tag{A.14}$$

$$\begin{aligned}\lambda_0 &= u_k; \\ \frac{dv_k}{dt} &= 0\end{aligned}\tag{A.15}$$

$$\begin{aligned}\frac{dN_k}{dt} &= \frac{N_k (u_k h_{s,k} - u_i h_{i,k})}{\alpha_k h_k (u_k - u_i)} \frac{d\alpha_k}{dt} - \frac{N_k}{\rho_k h_k} \frac{d(\rho_k e_k)}{dt} \\ &= -\frac{n N_k \rho_k u_k (h_k - h_{s,k})}{r h_k}\end{aligned}\tag{A.16}$$

$$\begin{aligned}\frac{d(\rho_k e_k)}{dt} &= \frac{\rho_k h_k (u_k a_{s,k}^2 - u_i a_{i,k}^2) - \rho_k c_k^2 (u_k h_{s,k} - u_i h_{i,k})}{\alpha_k c_k^2 (u_k - u_i)} \frac{d\alpha_k}{dt} \\ &\quad - \frac{h_k}{c_k^2} \frac{dP_k}{dt} = \frac{n \rho_k u_k}{r} \left( \frac{h_k c_{s,k}^2 - h_{s,k} c_k^2}{c_k^2} \right)\end{aligned}\tag{A.17}$$

$$\begin{aligned}\lambda_+ &= u_k + c_k; \\ \frac{dP_k}{dt} &+ \frac{\rho_k (u_k a_{s,k}^2 - u_i a_{i,k}^2) + c_k (P_k - P_{s,k})}{\alpha_k (u_k - u_i + c_k)} \frac{d\alpha_k}{dt} + \rho_k c_k \frac{du_k}{dt} \\ &= -\frac{n}{r} [\rho_k u_k c_{s,k}^2 + c_k (P_k - P_{s,k})]\end{aligned}\tag{A.18}$$

$$\begin{aligned}\lambda_- &= u_k - c_k; \\ \frac{dP_k}{dt} &+ \frac{\rho_k (u_k a_{s,k}^2 - u_i a_{i,k}^2) - c_k (P_k - P_{s,k})}{\alpha_k (u_k - u_i - c_k)} \frac{d\alpha_k}{dt} - \rho_k c_k \frac{du_k}{dt} \\ &= -\frac{n}{r} [\rho_k u_k c_{s,k}^2 - c_k (P_k - P_{s,k})]\end{aligned}\tag{A.19}$$

## Bibliography

- [1] M. R. Baer and J. W. Nunziato, *Int. J. Multiphase Flow*, **12**, 861-889, (1986).
- [2] J.B. Bdzil, R. Menikoff, S.F. Son, A.K. Kapila, and D.S. Stewart, *Phys. Fluids* **11** (2), 378 (1999).
- [3] J. R. Carney and J. M. Lightstone, (Personal communication, 2008).
- [4] C. Crowe, S. Sommerfield, and Y. Tsuji, *Multiphase Flows with Droplets and Particles* (CRC Press, 1998).
- [5] S.F. Davis, *SIAM J. Sci. Stat. Comput.* **9** (3),445 (1988).
- [6] R. Di Felice, *Intl. J. Multiphase Flow*, **20**, 153 (1994).
- [7] S. Ergun, *Chem. Eng. Prog.*, **48**, 89 (1952).
- [8] D. Gidaspow, *Multiphase Flow and Fluidization* (Academic Press, 1994).
- [9] S.K. Godunov, *Math. Sb.* **47**, 357-393 (1959).
- [10] K.A. Gonthier and J.M. Powers, *J. Comput. Phys*, **163**, 376-443 (2000).
- [11] E.S. Hertel and G.I. Kerley, CTH Reference Manual: The Equation of State Package, Technical Report SAND98-0947, Sandia National Laboratory (Albuquerque, NM, 1998).
- [12] A. Harten, P.D. Lax, and B. van Leer, *SIAM Review*, **25**, 33-61 (1983).

- [13] A.K. Kapila, R. Menikoff, J.B. Bdzil, S.F. Son, and D.S. Stewart, *Phys. Fluids* **13** (10), 3002 (2001).
- [14] E. Lee, M. Finger, and W. Collins, JWLEquation of State Coefficients for High Explosives, Technical Report UCID-16189, Lawrence Radiation Laboratory (Berkeley, CA, 1973).
- [15] R.J. Leveque, *Finite Volume Methods for Hyperbolic Problems* (Cambridge University Press, 2002).
- [16] T.P. McGrath II, J.R. Carney, and J.M. Lightstone, Numerical and Experimental Investigations of Multiphase Explosions with Inert Particles, 42nd JANNAF Combustion Symposium (Newton, MA, May 12-16 2008).
- [17] M.V. Papalexandris, *J. Fluid Mech.*, **507**, 95-142 (2004).
- [18] M.V. Papalexandris, *Combust. Flame*, **141**, 216-228 (2005).
- [19] W.E. Ranz and W.R. Marshall, *Chem. Eng. Prog.*, **48**, 141 (1952).
- [20] W.E. Ranz and W.R. Marshall, *Chem. Eng. Prog.*, **48**, 173 (1952).
- [21] J.F. Richardson and W.N. Zaki, *Trans. Inst. Chem. Engrs.*, **32**, 35-53 (1954).
- [22] P.N. Rowe, *Trans. Inst. Chem. Engrs.*, **39**, 175-180 (1961).
- [23] P.L. Rowe, *J. Comput. Phys.*, **43**, 357 (1981).
- [24] P.L. Rowe and J. Pike, Efficient construction and utilization of approximate Riemann solutions, in *Computing Methods in Applied Sciences and Engineering VI* (North-Holland, New York, 1984) p.499.
- [25] R. Saurel and O. Lemetayer, *J. Fluid Mech.*, **431**, 239-271 (2001).

- [26] J. Shepherd and D. Begeal, Transient Compressible Flow in Porous Materials, Technical Report SAND83-1788, Sandia National Laboratory, (Albuquerque, NM, 1983).
- [27] G. Strang, *SIAM J. Num. Analysis*, **5**, 506-517 (1968).
- [28] G. Tedeschi, H. Gouin, and M. Elena, *Experiments in Fluids*, **26**, 288-296 (1999).
- [29] E.F. Toro, *Riemann Solvers and Numerical Methods for Fluid Dynamics (2nd edition)*, (Springer-Verlag, 1999).
- [30] A.B. Wardlaw, J.A. Luton, J.R. Renzi, K.C. Kiddy, and R.M. McKeown, The Gemini Euler Solver for the Coupled Simulation of Underwater Explosions, Technical Report IHTR 2500, Indian Head Division, Naval Surface Warfare Center, (Indian Head, MD, 2003).
- [31] C.Y. Wen and Y.H. Yu, Mechanics of Fluidization. *Chem. Engr. Prog. Symp. Series*, **62**, 100-111 (1966).
- [32] F. Zhang, D.L. Frost, P.A. Thibault, and S.B. Murray, *Shock Waves*, **10**, 431-443 (2001).